



<b>Publication Year</b>	2018
<b>Acceptance in OA@INAF</b>	2021-01-11T09:11:19Z
<b>Title</b>	The SURvey for Pulsars and Extragalactic Radio Bursts - I. Survey description and overview
<b>Authors</b>	Keane, E. F.; Barr, E. D.; Jameson, A.; Morello, V.; Caleb, M.; et al.
<b>DOI</b>	10.1093/mnras/stx2126
<b>Handle</b>	<a href="http://hdl.handle.net/20.500.12386/29626">http://hdl.handle.net/20.500.12386/29626</a>
<b>Journal</b>	MONTHLY NOTICES OF THE ROYAL ASTRONOMICAL SOCIETY
<b>Number</b>	473

# The SURvey for Pulsars and Extragalactic Radio Bursts – I. Survey description and overview

E. F. Keane,<sup>1,2,3★</sup> E.D. Barr,<sup>2,4</sup> A. Jameson,<sup>2,3</sup> V. Morello,<sup>2,3</sup> M. Caleb,<sup>2,3,5</sup>  
S. Bhandari,<sup>2,3</sup> E. Petroff,<sup>2,3,6,7</sup> A. Possenti,<sup>8</sup> M. Burgay,<sup>8</sup> C. Tiburzi,<sup>4,9</sup> M. Bailes,<sup>2,3</sup>  
N. D. R. Bhat,<sup>3,10</sup> S. Burke-Spolaor,<sup>11</sup> R.P. Eatough,<sup>4</sup> C. Flynn,<sup>2</sup> F. Jankowski,<sup>2,3</sup>  
S. Johnston,<sup>7</sup> M. Kramer,<sup>4,12</sup> L. Levin,<sup>12</sup> C. Ng,<sup>4,13</sup> W. van Straten<sup>2</sup>  
and V. Venkatraman Krishnan<sup>2,3</sup>

<sup>1</sup>SKA Organisation, Jodrell Bank Observatory, Macclesfield SK11 9DL, UK

<sup>2</sup>Centre for Astrophysics and Supercomputing, Swinburne University of Technology, Mail H30, PO Box 218, VIC 3122, Australia

<sup>3</sup>ARC Centre of Excellence for All-sky Astrophysics (CAASTRO), Sydney

<sup>4</sup>Max-Planck-Institut für Radioastronomie, Auf dem Hügel 69, D-53121 Bonn, Germany

<sup>5</sup>Research School of Astronomy and Astrophysics, Australian National University, ACT 2611, Australia

<sup>6</sup>ASTRON, the Netherlands Institute for Radio Astronomy, Postbus 2, NL-7990 AA Dwingeloo, the Netherlands

<sup>7</sup>CSIRO Astronomy and Space Science, Australia Telescope National Facility, PO Box 76, Epping, NSW 1710, Australia

<sup>8</sup>INAF – Osservatorio Astronomico di Cagliari, Via della Scienza 5, I-09047 Selargius (CA), Italy

<sup>9</sup>Fakultät für Physik, Universität Bielefeld, Postfach 100131, D-33501 Bielefeld, Germany

<sup>10</sup>International Centre for Radio Astronomy Research, Curtin University, Bentley, WA 6102, Australia

<sup>11</sup>National Radio Astronomy Observatory, Socorro, NM 87801, USA

<sup>12</sup>Jodrell Bank Centre for Astrophysics, School of Physics and Astronomy, The University of Manchester, Manchester M13 9PL, UK

<sup>13</sup>Department of Physics and Astronomy, University of British Columbia, 6224 Agricultural Road, Vancouver, BC V6T 1Z1, Canada

Accepted 2017 August 14. Received 2017 August 11; in original form 2017 June 14

## ABSTRACT

We describe the Survey for Pulsars and Extragalactic Radio Bursts (SUPERB), an ongoing pulsar and fast transient survey using the Parkes radio telescope. SUPERB involves real-time acceleration searches for pulsars and single-pulse searches for pulsars and fast radio bursts. We report on the observational set-up, data analysis, multiwavelength/messenger connections, survey sensitivities to pulsars and fast radio bursts and the impact of radio frequency interference. We further report on the first 10 pulsars discovered in the project. Among these is PSR J1306–40, a millisecond pulsar in a binary system where it appears to be eclipsed for a large fraction of the orbit. PSR J1421–4407 is another binary millisecond pulsar; its orbital period is 30.7 d. This orbital period is in a range where only highly eccentric binaries are known, and expected by theory; despite this its orbit has an eccentricity of  $10^{-5}$ .

**Key words:** methods: data analysis – methods: observational – surveys.

## 1 INTRODUCTION

In the past decade, exploration of the high-time resolution radio Universe has begun to accelerate. This has resulted in numerous discoveries with high scientific impact (Hyman et al. 2005; Kramer et al. 2006; McLaughlin et al. 2006; Hallinan et al. 2007; Lorimer et al. 2007; Osten & Bastian 2008; Horeh et al. 2015; Bannister et al. 2016). This exploration is ever more tractable due to continuing technical developments in telescope observing infrastructure and in computing hardware and software. Some of the most exciting objects of study necessitate real-time searches

where the lag between the signal being received by the telescope and being identified in a search algorithm is reduced to the minimum possible; the reaction time typically needs to be of the order of the event duration. Millisecond time-scale signals such as pulsars and fast radio bursts (FRBs) are thus quite technically challenging.

The High Time Resolution Universe South (HTRU-S; Keith et al. 2010) survey has, between 2008 and 2014, performed a southern-sky search for pulsars and fast transients. Amongst its pulsar discoveries, HTRU-S identified the first ever magnetar discovered in the radio (Levin et al. 2010), the so-called diamond planet (Bailes et al. 2011) and identified new high timing precision pulsars (see e.g. Keith et al. 2011). Also due to its frequency resolution, HTRU-S expanded the pulsar search parameter space

\* E-mail: [e.keane@skatelescope.org](mailto:e.keane@skatelescope.org)

into regions of high dispersion measure (DM) and fast spin periods (Levin et al. 2013). The work of HTRU-S also confirmed the existence of the cosmological population of FRBs (Thornton et al. 2013), initially signalled by the discovery of the ‘Lorimer Burst’ (Lorimer et al. 2007).

Due primarily to limited computing resources in the past, the discovery lag for pulsar and FRB signals has been anywhere from months to several years. HTRU-S, like almost all previous pulsar and fast transient surveys, was subject to this. However, with the advent of fast networking capabilities between telescope hardware and supercomputers, and the ubiquity of multi- and many-core processors (Bardell, Barnes, & Fluke 2010), it is now possible to process data orders of magnitude faster. Applying these techniques provides an improvement over the HTRU-S survey, whereby new discoveries made with the Parkes telescope can be acted upon in real time. In the case of FRBs, a real-time discovery enables the preservation of more information about the burst and allows rapid action (or reaction) to determine the source of the burst. This would help identify the many basic properties of this population which remain unknown such as what their all-sky/latitude dependent rate is, their spectra, their brightness distribution and whether they are standard candles. Real-time pulsar searches are equally essential but for a very different reason. Due to the volume of data collected in pulsar searches, long-term storage becomes a critical problem. With high data rates and large surveys, there is no time to search offline in order to catch up. In the case of future telescopes such as the Square Kilometre Array (Braun et al. 2015; Kramer & Stappers 2015), offline searches will not be possible as not all data will be recorded in long-term storage. Real time pulsar searches can also open up new possibilities, where one would want to take advantage of time-dependent detectability. For example one could re-observe promptly if a pulsar is boosted in flux density due to interstellar scintillation, if a pulsar in a binary is found in a favourable part of the orbit, or if an intermittent pulsar is emitting for only a small fraction of the time.

In this paper, we describe the SURvey for Pulsars and Extragalactic Radio Bursts (SUPERB) that aims to perform acceleration searches for pulsars and single-pulse searches for FRBs (and pulsars) in real time, bringing the discovery lag down to seconds. Furthermore, SUPERB employs a network of multimessenger telescopes working with the Parkes Telescope, the primary telescope for the project. The search for pulsars covers the widest acceleration range ever for a real-time search and is thus in effect a demonstrator for what will be run on next generation telescopes. In Section 2, we give an overview of the project, the survey strategy and new software and hardware innovations employed. Section 3 describes the data acquisition and pipeline processing performed, and Section 4 outlines the multimessenger synergies with other facilities across the electromagnetic spectrum and in other windows. The first pulsar discoveries from the project are described in Section 5, with particular focus on key interesting individual objects. Finally, we summarize in Section 6.

## 2 OVERVIEW

In this section we describe the survey strategy for SUPERB.

With the suggested latitude dependence in the detectable FRB rate seen in the HTRU Mid Latitude survey (Petroff et al. 2014), albeit subject to low-number statistics, it was decided to initially focus on a ‘high’ Galactic latitude region  $15^\circ < |b| < 25^\circ$  (as indicated by the previous analyses) to explore the cut-off of this effect. As the survey progressed, it was discovered that this latitude dependence appears

to become evident at even higher latitudes. The FRB rate seems to increase above  $|b| \sim 40\text{--}50^\circ$ , apparently by as much as a factor of  $\sim 3$ , albeit with this also being subject to small number statistics; this will be discussed further in the second paper in this series by Bhandari et al. (2017), hereafter *Paper II*. With this information, it was decided to increase the latitude range of the survey. A survey extension over the initial sky region, dubbed SUPERBx,<sup>1</sup> was undertaken to go all the way to the Southern Galactic pole and, on the other side of the Galactic plane, to  $b = 45^\circ$ . In addition to these FRB-motivated selections in Galactic latitude, sections through the Galactic plane previously not covered to depths of 9-min observations were included to specifically search for pulsars that would have been missed by previous studies (in particular HTRU-S). With the above selections in Galactic latitude, the longitude range was essentially set by the sky visible at Parkes. Despite the limited time on sky available, pointings in the Northern Celestial hemisphere were not excluded so as to (a) maximize overlap with multiwavelength facilities (see Section 4), and (b) to enable future cross-calibration with pulsar surveys running at other radio telescopes in the Northern hemisphere.

Some of the region covered by SUPERB has been covered previously with the same data-acquisition (but not data-processing, see Section 3) set-up, using 4.5-min pointings in the high-latitude component of the HTRU-S survey. The benefits of a second pass (or multiple passes) of the same area of sky are many, when it comes to pulsar searches: (i) intermittent pulsars that can be ‘off’ more often than not (Kramer et al. 2006), usually strongly selected against, become detectable; (ii) when looking at high Galactic latitudes in particular, there is more scintillation as pulsar signals can be boosted in their apparent brightness due to focusing in the turbulent interstellar medium (Rickett 1970) and (iii) pulsars may be detected in parts of binary orbits where they are not being eclipsed (Lyne et al. 1990) or, for the most extremely relativistic systems, in parts of the orbit where the acceleration is within the search range. On top of these benefits, one can leverage real-time processing pipelines to realize that the optimal time to re-observe a pulsar (or a pulsar candidate) is right now. Typical processing lags in the past meant that attempted follow-up observations days or weeks later were often unsuccessful requiring repeated attempts to confirm pulsar candidates. Doing this correctly and routinely also results in more efficient use of telescope time. From the point of view of single-pulse searches, multiple passes provide a longer time on sky increasing the likelihood that (i) a pulsar of any period exhibits a pulse at the bright end of its pulse amplitude distribution; and (ii) a sufficient number of pulse periods of a long-period pulsar occur during the observation. Long-period pulsars are strongly selected against in both periodicity and single-pulse searches, but the situation improves with observing time. For FRBs that, in all but one case so far (Spitler et al. 2016), are not seen to repeat, these benefits do not apply. For these sources, excepting the hinted-at latitude dependence, the current thinking is that it does not matter where we point so that  $N$  pointings of  $M$ -minute duration are just as good as performing a single  $N \times M$ -minute pointing. Practically one loses time doing the former as even the ideal case where there is no radio frequency interference (RFI) and weather conditions are favourable one must always slew between pointings, but it is only the former that allows a sensible simultaneous pulsar

<sup>1</sup> The SUPERB project is split across two project IDs in the Parkes data archive: P858 and P892. To obtain all the data, as described in the Data Access section at the end of this paper, one should query both of these project IDs.

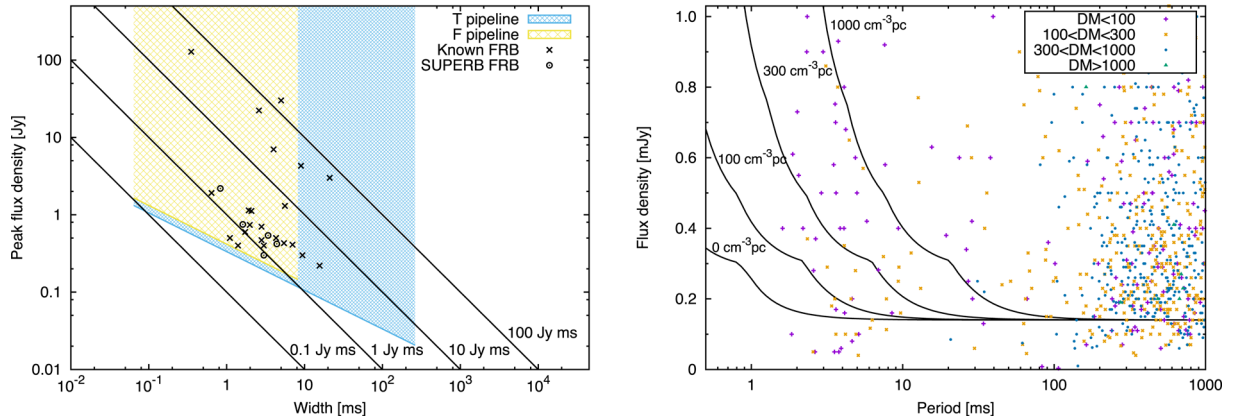


**Figure 1.** Left: single-pulse search sensitivity plot for the SUPERB survey. Overplotted are the 27 known FRBs with the relevant parameters published, including the five SUPERB discoveries (see the FRB Catalogue of Petroff et al. 2016, Keane et al. 2016 and Paper II for more details). Right: periodicity search sensitivity plot for the SUPERB survey with the known pulsar population overplotted in subgroups (denoted by different symbols and colours) divided by their DM values.

search, except for a strategy where one might stare at a globular cluster such as 47 Tucanae (Robinson et al. 1995) or Terzan 5 (Ransom 2005).

With SUPERB, we decided to perform 9-min pointings, deeper than previous HTRU-S observations that covered some of the SUPERB sky region. Furthermore, the SUPERB pointings are ‘in between’ previous pointings in two senses: (i) in tessellating the sky we first placed the most sensitive central beam of the Parkes multibeam receiver in locations covered previously by the least sensitive outer-ring beams; and (ii) we further offset the pointings by half of a half-power beamwidth so that points previously at the half-power point were now on-axis and vice-versa. These steps allow a more complete sampling of the pulsar luminosity distribution. Repeating the same pointing locations would repeat the incomplete coverage of the luminosity function. In this way, pulsars that fell into such ‘gaps’ in previous studies can now be detected. Fig. 1 shows the sensitivity of SUPERB for both periodicity and single-pulse searches.

The first SUPERB observing run was in 2014 April and lasted for 2 d. Subsequently, it ran with some regularity from 2014 July to 2016 January. 2016 January to late 2016 saw a hiatus as Parkes was used primarily to commission a phased-array-feed (Deng et al. 2017), but SUPERB resumed observations from 2016 December. In this first paper, we consider the results up to the end of 2016 January. The major observing parameters are outlined in Table 1 and the motivations for these choices are given below. Additionally, the entire list of survey pointings performed to the end of January 2016, illustrated in Fig. 2, is included in the additional online material associated with this article.

### 3 INFRASTRUCTURE

One of the core objectives of SUPERB is to enable real-time pulsar and FRB searches. Thus, it requires comprehensive infrastructure with minimal human input to allow for automated operation. Below, we describe the data acquisition, processing pipelines and data management scheme used in the project, which is shown schematically in Fig. 3.

#### 3.1 Data acquisition

SUPERB uses a modified version of the observing system described by Keith et al. (2010). Here, the Berkeley Parkes Swinburne

**Table 1.** Observational parameters of the survey. In case two values are given, the first is for SUPERB (P858) and the second is for the SUPERBx (P892) components of the project.

Parameter	Value
Regions (P858)	$-120^\circ < l < 50^\circ$ , $15^\circ <  b  < 25^\circ$ $29^\circ < l < 50^\circ$ , $-25^\circ < b < 25^\circ$
Regions (P892)	$-140^\circ < l < 50^\circ$ , $25^\circ < b < 45^\circ$ $-140^\circ < l < 50^\circ$ , $-30^\circ < b < -25^\circ$ $-140^\circ < l < 50^\circ$ , $b < -45^\circ$ $-140^\circ < l < -120^\circ$ , $-25^\circ < b < 25^\circ$
$\tau_{\text{obs}}$ (s)	$\sim 560$
$N_{\text{beams}}$ (planned)	86 424 and 180 583
$N_{\text{beams}}$ (observed)	71 572 and 141 512
$T_{\text{samp}}$ ( $\mu\text{s}$ )	64
$\Delta\nu$ (MHz)	400
$\Delta\nu_{\text{chan}}$ (kHz)	390.625
$N_{\text{chans}}$	1024
$N_{\text{samples}}$	$\sim 2^{23}$
$N_{\text{bits}}$ (online search)	2 (periodicity), 8 (single pulse)
$N_{\text{bits}}$ (offline search)	2
$N_{\text{bits}}$ (archival)	2
Archived data (TB)	154 and 303

Recorder (BPSR) backend is used to digitize, filterbank, detect and temporally average the signal from each beam of the Parkes 21-cm multibeam receiver (Staveley-Smith et al. 1996). The output from BPSR is an 8-bit, full-Stokes filterbank with 1024 frequency channels spanning 400 MHz of bandwidth (1182–1582 MHz) and  $64\text{-}\mu\text{s}^{-1}$  time resolution. As noted by Keith et al. (2010), the effective bandwidth is  $\sim 340$  MHz due to the presence of strong RFI from communication satellites emitting in the 1525–1559 MHz band and roll-off at the band edges (see Section 5.4). The output from BPSR is sent to the HTRU-Pulsar Signal Processor (HIPSR; Price et al. 2017) backend for further processing. It is here that the observing systems of HTRU-S and SUPERB diverge. Where previously data arriving in HIPSR would have been bit-compressed and the Stokes I component written to disc and thence to magnetic tape, for the SUPERB survey the data are instead pushed into a 120-s ring buffer. This ring buffer serves two purposes; it provides input to a real-time transient search and it enables full-Stokes data to be recorded upon receipt of a trigger. Following the transient search, the Stokes I component of the data is bit-compressed to 2 bits per sample and is written

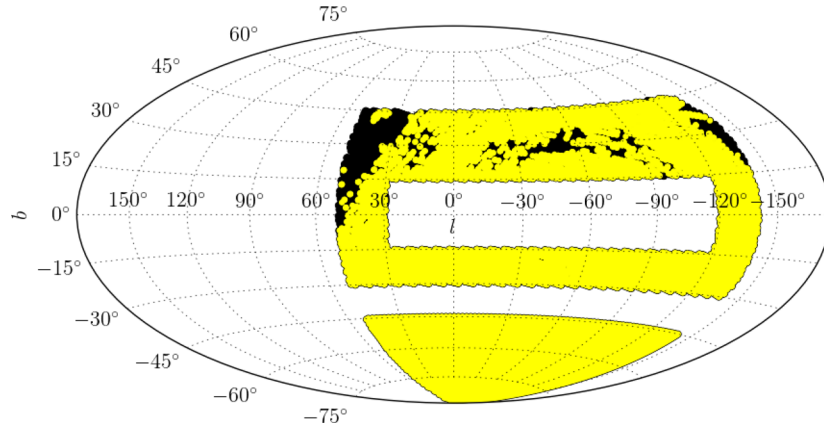


**Figure 2.** An Aitoff projection of the sky in Galactic coordinates. Those regions covered with 9-min SUPERB pointings are marked in yellow. Pointings planned, but not yet observed before the end of January 2016 are marked in black.

to disc on HIPSr. The removal of the magnetic tape storage step, employed by HTRU-S and previous surveys, is significant as the writing of data to tape had been the major contributing factor in discovery lag.

### 3.2 Processing hardware

Upon completion of an observation at Parkes, the data are streamed from the HIPSr backend to the Green II (G2) supercomputing cluster located at the Swinburne University of Technology. The G2 is composed of three main components, the SwinSTAR and gSTAR compute clusters and a  $\sim 5$  PB lustre file system. For the purposes of SUPERB data processing, we are primarily interested in the number of GPUs available on each cluster, to wit whether SwinSTAR provides 47 nodes each with two six-core X5650 CPUs, 48 GB of RAM and two Nvidia Tesla C2070 GPUs; and gSTAR provides 61 nodes each with two eight-core E5-2660 CPUs, 64 GB RAM and a Nvidia Tesla K10 GPU. SwinSTAR further provides three high-density nodes, each with two six-core X5650 CPUs, 48 GB RAM and seven Tesla M2090 GPUs. G2 uses a PBS-based queue system, employing Torque and Moab for resource management and job scheduling, respectively.

### 3.3 Processing pipelines

Data observed as part of SUPERB are searched for both periodic and transient signals. In both cases, the data go through both a fast (F) and thorough (T) version of the respective processing pipeline. The objective of the F pipeline processing is to enable real-time processing, picking up the brighter signals with less extreme properties, while the objective of the T pipeline processing is to maximize our chances of discovery by searching a larger volume of parameter space with higher resolution. Below, we describe the F and T versions of both our periodicity and transient searches, which is shown schematically in Fig. 4.

#### 3.3.1 Transient search pipeline

While the data are still stored in the 120-s ring buffer on the HIPSr system, they are searched using the F pipeline for single pulses while still at 8-bit precision. This pipeline uses the HEIMDALL<sup>2</sup> software

package to search 16-s segments (or ‘gulps’) of incoming data<sup>3</sup> over a range of pulse widths, and DMs for signals with properties resembling those of real astrophysical pulses. The F pipeline search is restricted to 1623 DM trials between 0 and  $2000 \text{ pc cm}^{-3}$  and 13 width trials between 0.064 and 262.144 ms. The maximum DM was in 2015 December, increased to  $3000 \text{ pc cm}^{-3}$ . The search is run on each beam individually to produce a list of candidates that are then cross-correlated between beams to eliminate local RFI that occurs uniformly, or in non-neighbouring beams. Frequency channels of known sources of RFI are masked during the search to limit contamination. Several cuts, described in the following section, are applied to the resulting candidates for each gulp to search for FRBs; the list of single-pulse candidates is not saved to disc.

After a pointing is completed the data are saved as filterbank files and sent to the gSTAR supercomputer at Swinburne, they are searched again for single pulses using the T pipeline. This pipeline is an expanded version of the F pipeline on HIPSr which searches an entire pointing over a larger parameter space to ensure that no viable candidates are missed. For the T pipeline, the pointing is searched up to a maximum DM of  $10\,000 \text{ pc cm}^{-3}$  using 1986 DM trials, and searched for pulses up to a maximum width of 262.144 ms. The beams are processed in a similar manner to the F pipeline, i.e. individually and then compared to remove coincident RFI. Additional RFI excision occurs in the form of frequency masking (as with the F pipeline) and an eigenvector decomposition based algorithm (Kocz, Briggs & Reynolds 2010). The list of single-pulse candidates are, in this case, saved to disc.

#### 3.3.2 Transient candidate selection

After running the F and T pipelines, the above parameters produce a sizeable number of candidates. These are parsed according to the following rules. In the F pipeline, we apply

$$\begin{aligned} \text{DM} &\geq 1.5 \times \text{DM}_{\text{Galaxy}} \\ \text{S/N} &\geq 10 \\ N_{\text{beams,adj}} &\leq 4 \\ W &\leq 8.192 \text{ ms} \\ N_{\text{events}}(t_{\text{obs}} - 2 \text{ s} \rightarrow t_{\text{obs}} + 2 \text{ s}) &\leq 5, \end{aligned} \quad (1)$$

<sup>3</sup> The size of these gulps is configurable; 16 s is the default value used in SUPERB’s pipelines.

<sup>2</sup> <http://sourceforge.net/projects/heimdall-astro/>



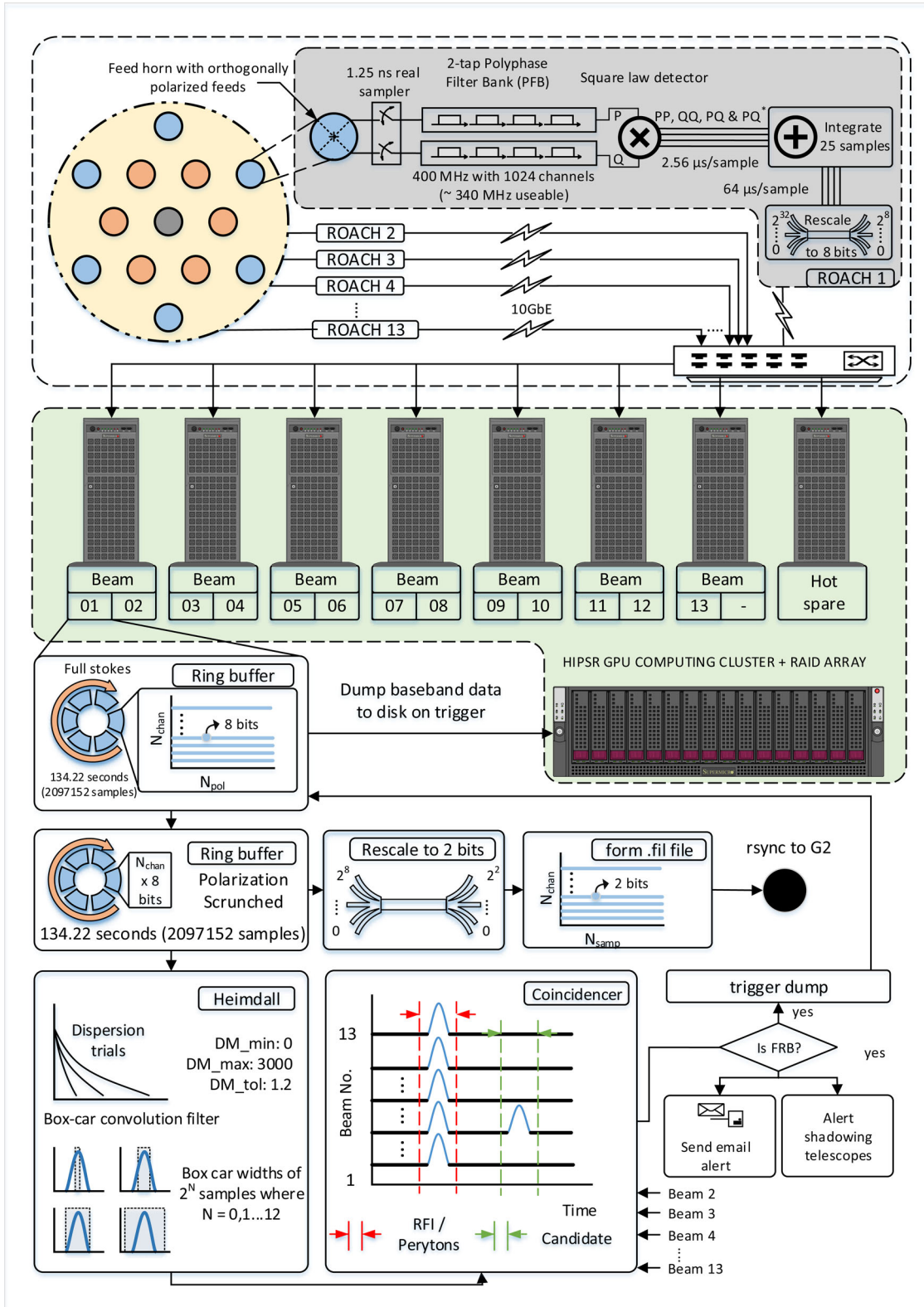


**Figure 3.** A schematic of the SUPERB acquisition and data analysis pipeline. The topmost block shows the Parkes primary beam (yellow) with the 13-beam pattern of the multibeam receiver overplotted. Each beam is processed separately in the same way (grey block) on a Roach field programmable gate array – Nyquist sampled in two orthogonal polarizations, formed into a filterbank, square-law detected to polarization products and integrated down in time, rescaled from 32 bits to 8, then transferred to a GPU-enabled computing cluster for further searching (green block). The F pipeline single-pulse search happens on these machines – a ring buffer in memory is searched for dispersed pulses satisfying several criteria (see main text) to identify these as FRB candidates. *Bona fide* FRB candidate information is sent to other telescopes for data dumps (for shadowing telescopes) and/or follow-up.

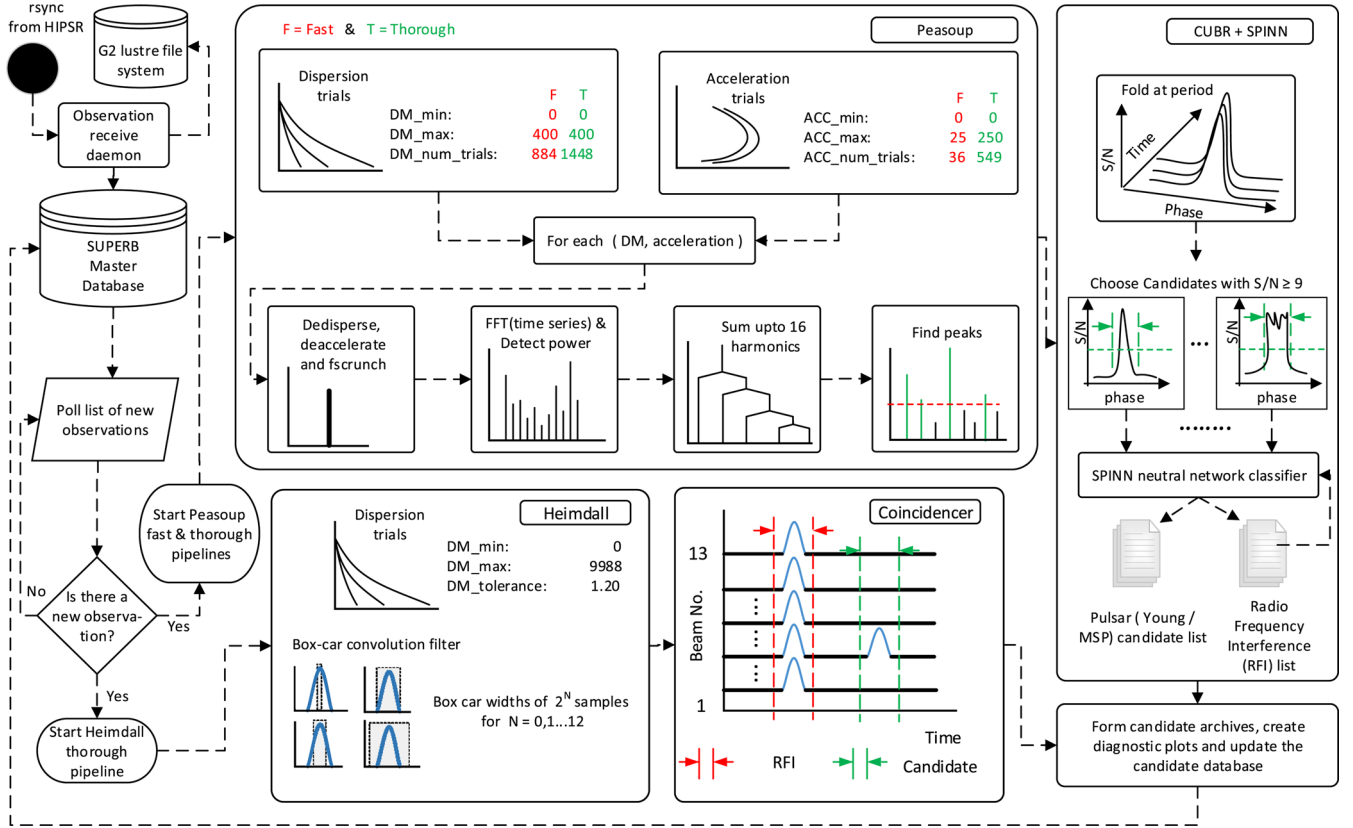


Figure 4. A schematic of the SUPERB processing pipelines on gSTAR.

where DM and  $DM_{\text{Galaxy}}$  are the DM of the candidate and the modelled DM contribution from the Milky Way from the NE2001 model (Cordes & Lazio 2002), respectively, S/N is the signal-to-noise ratio of the candidate,  $N_{\text{beams,adj}}$  is the number of adjacent beams in which the candidate appears,  $W$  is the width of the candidate pulse and the final cut describes the number of candidates detected within a 4-s window centred on the time of the candidate. If there are too many candidates in a time region around the candidate of interest it is ignored, a precaution to reduce the number of false positives due to RFI. The F pipeline only searches for pulses from FRBs, hence the high-DM cut-off for viable candidates. The excess DM factor of 1.5 is arbitrary and might conceivably result in missed FRBs in the F pipeline (or initial classification of an FRB as an RRAT, see Keane 2016).

In the T pipeline, the data are searched for single pulses from pulsars as well as pulses from FRBs to ensure that no candidates are missed in the full processing of the data. For the T pipeline, we apply

$$\begin{aligned}
 DM &\geq 2 \text{ pc cm}^{-3} \\
 S/N &\geq 8 \\
 N_{\text{beams}} &\leq 4 \\
 W &\leq 262.144 \text{ ms},
 \end{aligned} \tag{2}$$

where the parameters are as in equation (1). The T pipeline processing is intended to detect lower S/N FRBs and single pulses from pulsars (see Fig. 5).

### 3.3.3 Periodicity searching

Periodicity searching of the SUPERB survey is performed using the GPU-enabled pulsar searching code, PEASOUP.<sup>4</sup> To implement a real-time pipeline, the three high-density gSTAR nodes (21 Tesla M2070 GPUs) were reserved for all SUPERB observing sessions. The search parameters are summarized in Table 2.

In both F and T pipelines, we fold all candidates detected by PEASOUP with an S/N higher than 9, and always fold the 24 brightest candidates of every beam. Fig. 6 shows an example of candidate diagnostic plots from the periodicity search. Motivated by the difficult RFI environment at Parkes and the constraint of real-time processing for the F pipeline, a folding software package named CUBR has been written for the survey. It can fold candidates in parallel, which reduces processing time by a factor of  $\sim 5$  as compared to equivalent tools in the PSRCHIVE package (Hotan, van Straten & Manchester 2004). It also has the ability to delete interference signals directly in the folded data; abnormal frequency channels or subintegrations are identified using an outlier detection method and the corresponding data are replaced by an appropriately chosen constant value. This has the benefit of reducing the difficulty of candidate evaluation, and in some cases identifies pulsars that would otherwise be entirely masked by interference (see Fig. 7). CUBR's RFI mitigation algorithms are described in length in Morello (2016).

<sup>4</sup> <https://github.com/ewanbarr/peasoup>

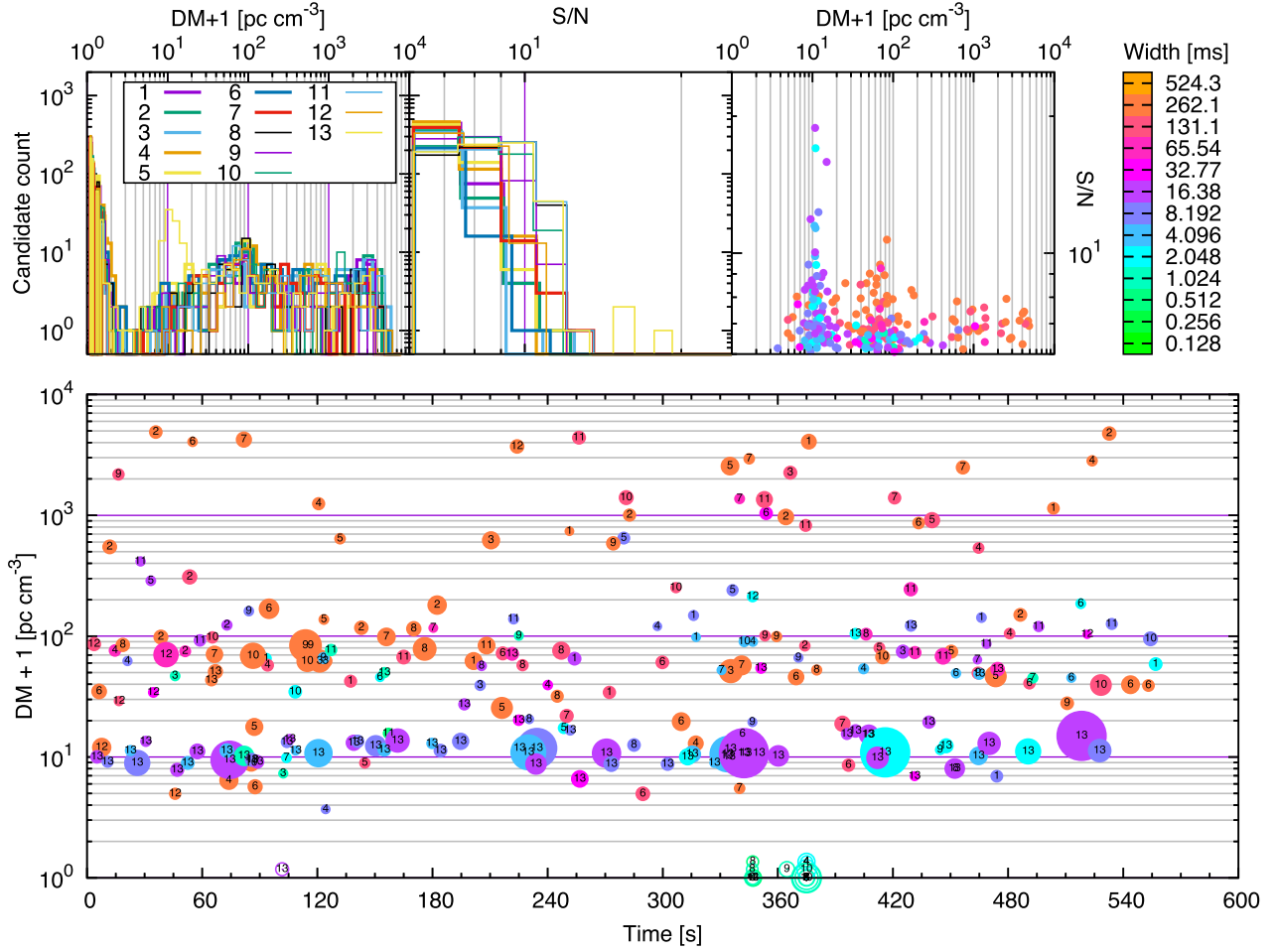


**Figure 5.** A single-pulse search candidate plot for a single SUPERB pointing. The top three panels show a histogram of events as a function of DM, then a histogram as a function of S/N, and a scatter plot of the DM and S/N of each candidate. The bottom plot shows the candidates in time and DM; here the colour corresponds to the pulse width and the number is the beam in which the candidate was detected. All candidates above an S/N of 8 are plotted here. In this example, several pulses are evident in beam 13 at a DM of approximately  $10 \text{ pc cm}^{-3}$ . We note that the bottom panel's axis label is  $\text{DM} + 1 \text{ pc cm}^{-3}$  rather than simply DM. The reason for this is that a base-10 logarithmic scaling is appropriate for our DM sampling, but there is still a need to display zero DM events to identify RFI. RFI signals peak at zero DM and depending on their time duration can be detected at higher DM values also.

**Table 2.** The processing parameters for the F and T transient and periodicity search pipelines.

Single-pulse pipeline parameter	F pipeline	T pipeline
DM range ( $\text{pc cm}^{-3}$ )	0–2000	0–9988
DM trials, $N_{\text{DM}}$	1623	1986
Width trials	$(1-2^{12}) \times t_{\text{samp}}$	$(1-2^{12}) \times t_{\text{samp}}$
RFI excision methods	Bad channels	Bad channels eigenvector excision
Periodicity search pipeline parameter	F pipeline	T pipeline
Maximum DM, $\text{DM}_{\text{max}}$ ( $\text{pc cm}^{-3}$ )	400	400
Trial DMs, $N_{\text{DM}}$	884	1448
Maximum acceleration, $ a_{\text{max}} $ ( $\text{m s}^{-2}$ )	25	250
Acceleration trials, $N_{\text{acc}}$	36	549
Number of harmonic folds performed, $N_h$	4	4
RFI excision methods	Bad channels Birdie list	Bad channels Birdie list Eigenvector excision

### 3.3.4 Periodicity candidate selection

The combined output rate of both periodicity search pipelines is approximately 4000 candidates per observed hour, and they have

generated a total of 5.9 million folded candidates so far. Visual inspection of all candidates is not a viable option considering the thousands of hours of tedium it would involve and more importantly the real-time discovery constraint we set for the F pipeline.



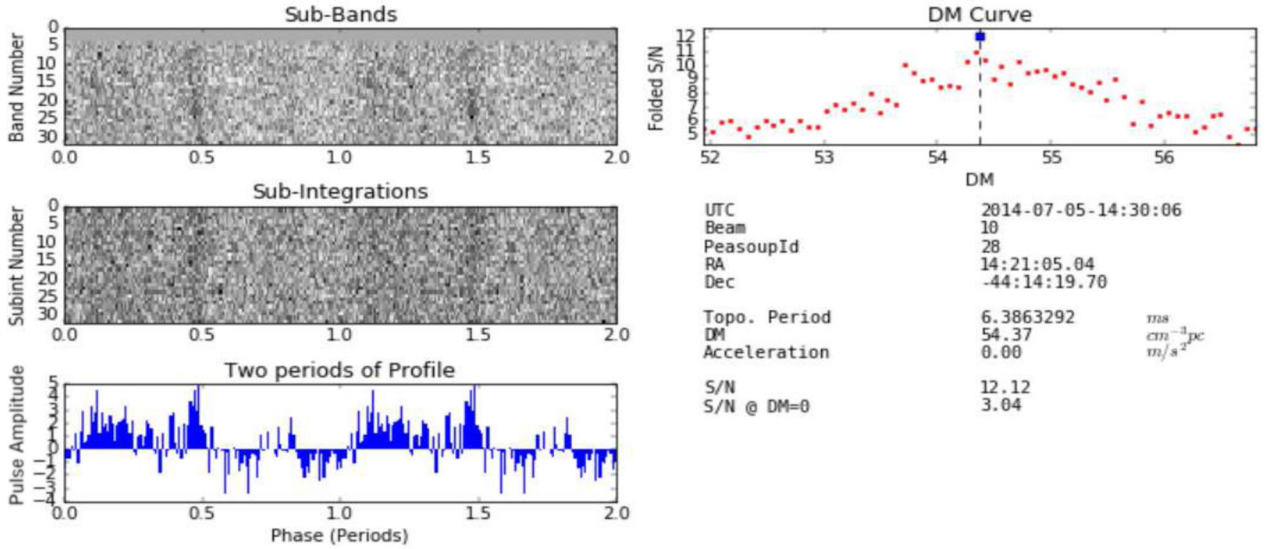


**Figure 6.** An example candidate plot from our pulsar searching pipeline: this is the first detection of PSR J1421–44. The panels shown are, in grey-scale, the period-folded signal as a function of frequency (top) and time (bottom), a folded pulse profile (blue profile) and a curve showing the S/N as a function of DM. Pertinent information about the pointing and candidate are also displayed. Diagnostic plots such as these are often used in examining candidates arising from our pipelines.

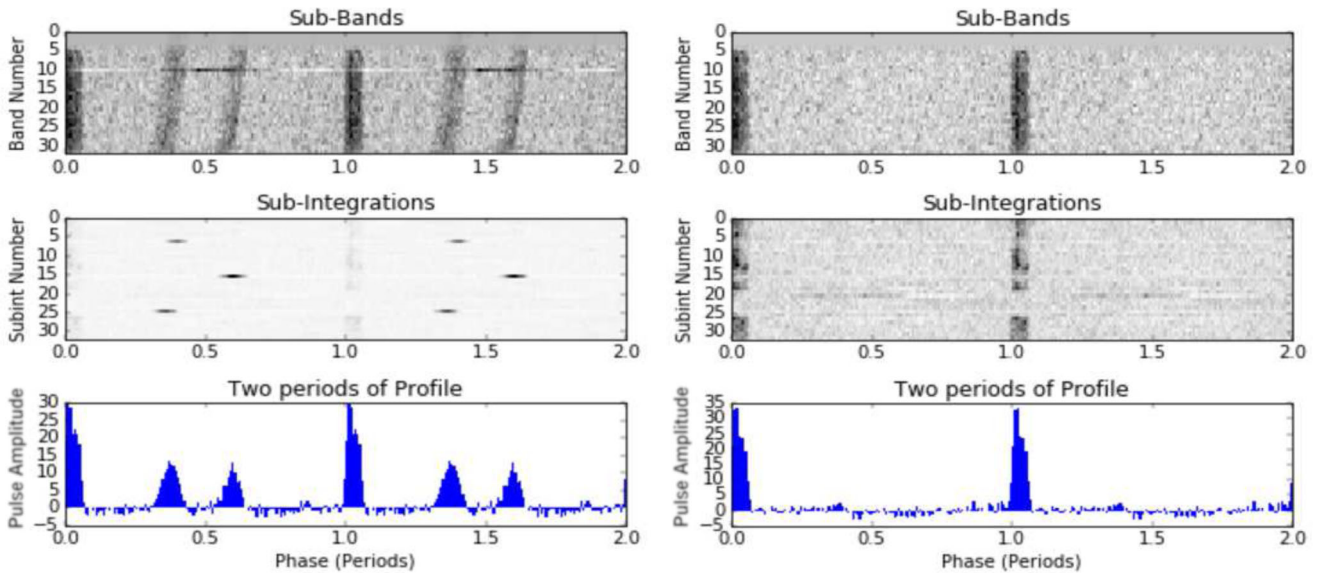


**Figure 7.** An observation of PSR J1759–1029 ( $P = 2.512$  s) before and after the application of the CUBR RFI mitigation algorithms. The pulsar’s signal is the vertical trail (two periods are shown for readability), and is demonstrably nulling in subintegrations 20 to 25. Top left panel: a strong, periodic sine-wave-like RFI is present in frequency band no. 10. Middle left panel: additionally, three bright dashes correspond to brief bursts of broad-band interference; they are also visible in the subbands plot as curved trails, and generate secondary pulses in the overall folded profile (bottom panel). Right column: the same plots after the application of interference mitigation algorithms.

We therefore entirely transferred the task of candidate selection to a machine learning algorithm. We use an improved version of the Straightforward Pulsar Identification Neural Network (SPINN) pulsar candidate classifier (Morello et al. 2014). It is an artificial neural network that evaluates candidates based on eight numerical features, and outputs a score between 0 and 1 that can be interpreted as the likelihood of being a pulsar.

SPINN was trained on a large sample of candidates obtained by running our search and folding pipeline on the HTRU-S Intermediate Latitude survey (Keith et al. 2010), which was observed between

2008 and 2010 with the same telescope, instrument, and sampling and integration times, but covered an area of the sky that does not overlap with that of SUPERB. We could therefore rigorously test the classification accuracy of SPINN on a sample of SUPERB candidates, knowing that none of those could have been ‘seen’ by the algorithm during training. Using the ephemerides published in the ATNF pulsar catalogue (Manchester et al. 1990), we manually identified every known pulsar detection found by PEASOUP during the first part of the survey (up to 2015 April). This gave us a test sample of 139 pulsar detections along with 1418 598 non-pulsar candidates

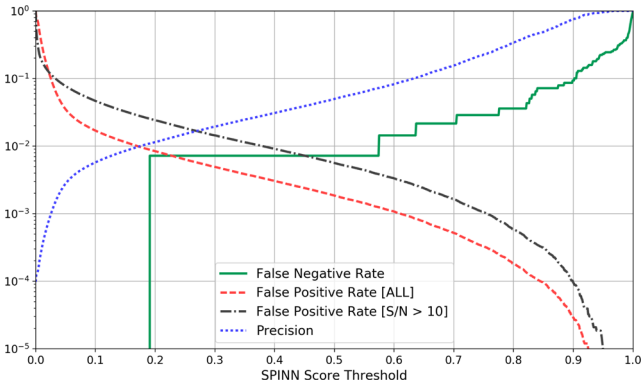


**Figure 8.** Classification error rates (log-scale) of SPINN as a function of output score selection threshold. The false negative rate is the fraction of pulsars missed (green line). The false positive rate is the fraction of spurious candidates incorrectly reported as pulsars (red line). We also evaluated it on the subset of candidates with  $S/N > 10$  (black line), since those cannot be trivially rejected by the classifier based on their lack of statistical significance. Precision (blue line), is the fraction of genuine pulsars contained in the sample of candidates selected by the classifier, a relevant metric for the real-time detection pipeline.

that were scored by our classifier. From there, we computed classification error rates as a function of score selection threshold; the results are summarized in Fig. 8.

We use different neural network score thresholds for the F and T pipeline. For real time discovery, we select candidates scoring higher than 0.85 to ensure a small false positive rate ( $\approx 1$  in  $10\,000$ ) so that discovery alerts are reliable and can be acted upon quickly. In the T pipeline, we value search completeness most highly and therefore tolerate a higher false positive rate at the cost of a longer round of visual candidate inspection; we typically inspected candidates down to a score of 0.5, and 0.4 for millisecond pulsar candidates. This involved looking at on order of  $10\,000$  candidate plots over the course of the entire survey.

### 3.3.5 Peryton pipeline

At the inception of the project, we planned to search for ‘perytions’ (Burke-Spolaor et al. 2011b). These transient signals had been detected in archival data from Parkes with more than a decade of discovery lag and, although clearly terrestrial in nature, their source had yet to be pinpointed as of 2014 when SUPERB was beginning. We searched for perytons as for transient events above but with two slight modifications. First, to take advantage of the fact that perytons are local and therefore detectable in most or all 13 beams of the receiver, the 13 beams are added to produce a new filterbank. Astrophysical events, which are typically in a single beam, are thus suppressed in  $S/N$  by a factor of  $\sqrt{13} \sim 3.6$ , whereas peryton signals are boosted by up to this factor in the resultant data set. This data is then searched as per the single-pulse search of a single beam. In identifying peryton candidates, the number-of-beams sifting rule does not apply, and no DM cut is applied. SUPERB thus has the ability to discover peryton events in real time and did this when they first occurred during SUPERB observations in 2015 January 2015. The combination of the ability to identify these signals without any discovery lag, and the data from the RFI monitor installed at Parkes in 2014 December allowed the source of the perytons to be identified. The simultaneous coverage up to 3 GHz allowed us to identify the carrier frequency of  $\sim 2.4\text{--}2.5$  GHz and through a process of deduction the culprit: unshielded microwave ovens on

site. This work is discussed in more detail in Petroff et al. (2015). Since this time a live peryton search is not routinely performed but the publicly available survey data still contain these signals should others wish to pursue this study.

### 3.3.6 Future pipelines

(i) *Fast folding search*: due to short observing lengths, the survey suffers a sensitivity loss to long-period pulsars that cannot be detected through their single pulses. It has long been known that the fast folding algorithm (FFA; Staelin 1969) offers the possibility to recover sensitivity to these pulsars, even in short and noisy observations. Due to its computationally intensive nature, the FFA has seen only sparse use in blind pulsar surveys to date (although it has seen use in targeted searches, see e.g. Kondratiev et al. 2009). However, renewed interest in FFAs (Cameron et al. 2017) and their implementation on many-core compute architectures has led to the development of new codes that can be applied to the SUPERB data set. The application of an FFA to SUPERB data will address known biases in our processing and greatly improve our capability to discover pulsars at the long-period extreme of the population. This pipeline commenced in 2017 April and the results of this will be reported at a later date.

(ii) *Low-level RFI mitigation algorithms*: in both the transient and periodicity search pipelines, most of the burden of RFI rejection is currently placed on the final candidate selection stage. This approach is not optimal since interference occurring during a pulsar observation can be strong enough to make the pulsar’s signal completely unrecognizable at the candidate inspection stage, even by a highly trained expert. In particular, a very common and unwelcome occurrence in SUPERB data is that of bright, broad-band non-dispersed pulses lasting several milliseconds that are simultaneously visible in all beams of the receiver. These negatively impact the detectability of slow pulsars in the Fourier domain and are a prolific source of false positives to the single-pulse search. Existing tools such as the *rfifind* routine of the PRESTO package (Ransom et al. 2002) do not effectively mitigate their effects. An attractive approach here is the application of spatial filtering (Leshem & van der Veen 2000; Raza & van der Veen 2002; Kocz et al. 2010), which is particularly efficient at identifying and cancelling any interfering signal present in a large number of beams; while normally applied to baseband data, we are currently investigating the use of spatial filtering on incoherent filterbanks, allowing its deployment on archival data.

## 4 MULTIWAVELENGTH SYNERGIES

The Parkes telescope is the primary instrument of the SUPERB project. However, it is joined in its search efforts for varying amounts of time by a number of additional facilities (see Table 3), some of which work simultaneously and some of which react to triggers from Parkes. In this section, we describe the shadowing (simultaneous observations) and triggering performed in the electromagnetic spectrum as well as multimessenger searches for counterparts to Parkes discoveries.

### 4.1 Shadowing

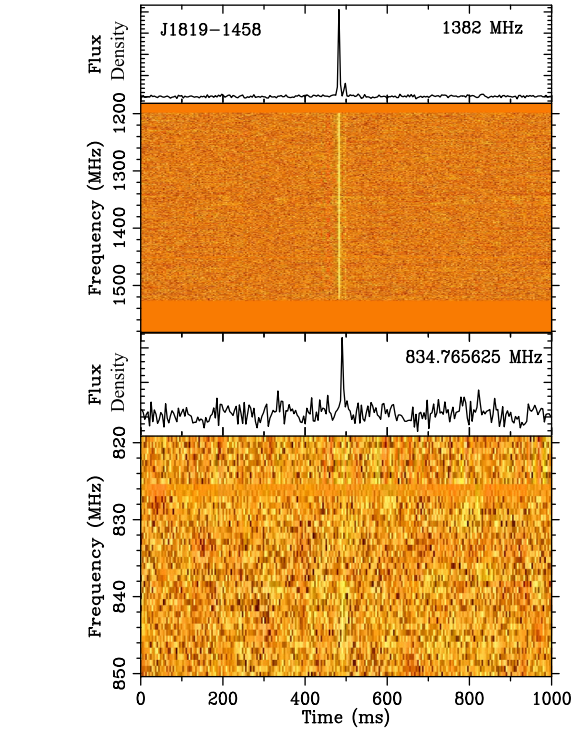
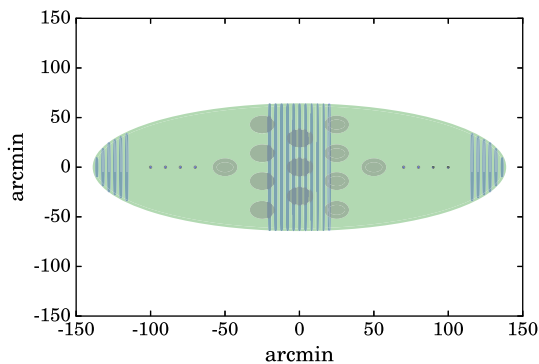
The observations at Parkes are shadowed to various degrees by other telescopes. At the time of writing, this has been done with the upgraded Molonglo Synthesis Telescope (UTMOST), the Giant

**Table 3.** The network of instruments alerted to SUPERB FRB triggers.

Telescope name	Band/filters
HESS	10 GeV–10 TeV
Swift	0.2–10 keV
Liverpool Telescope	<i>R</i>
Skymapper Telescope	<i>H<math>\alpha</math></i> , <i>ugvriz</i>
Zadko Telescope	<i>R</i>
Thai National Observatory	<i>R</i>
Blanco Telescope	<i>irVR</i>
Subaru Telescope	<i>r'i'i</i>
Keck Telescope	400–1100 nm
Magellan Telescope	<i>J</i>
MWA	185 MHz
GMRT	1.4 GHz, 610 MHz
Sardinia Radio Telescope	1.4 GHz
Effelsberg	1.4 GHz
ATCA	4–8 GHz

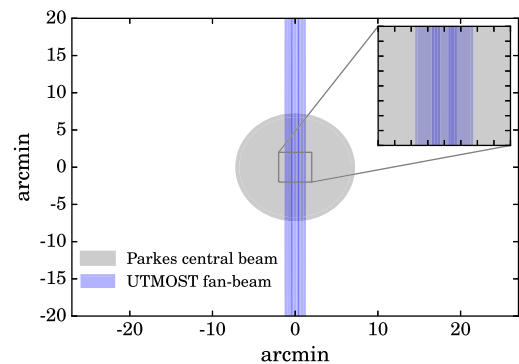
Metrewave Radio Telescope (GMRT) and the Murchison Widefield Array (MWA). At the conception of the SUPERB project in late 2013, the intention was to shadow Parkes with Molonglo at all times. By the start of the first SUPERB observing session in 2014 April, the shadowing infrastructure was in place, but the Molonglo upgrade was still in progress. Upon detection of an FRB, a ring buffer of the polarization power data at Parkes is dumped and a signal is sent to Molonglo to dump the single polarization complex voltage data from every module in the array. The idea is to detect the signal at both telescopes and, in the case of an FRB, localize the signal an order of magnitude more precisely than either telescope can do by itself and to obtain vital information on spectra. This concept is illustrated in Fig. 9.

Tests of this joint observing mode were performed using the erratic pulsar J1819–1458 (McLaughlin et al. 2006) which has a known spectrum and exhibits very bright pulses every  $\sim$ minute at 1.4 GHz at Parkes. The initial tests revealed that the sensitivity of Molonglo was less than 1 per cent of its final target sensitivity and as such Molonglo shadowing, though available, was not utilized for most of the observations reported here. However, in the interim the Molonglo upgrade has proceeded at pace, further tests with J1819–1458 were a resounding success (see Fig. 10), and the sensitivity is now at a level above 10 per cent of the theoretical optimum. This progress is well illustrated by the recent indepen-


**Figure 10.** First simultaneous detection of a pulse from J1819–1458 at Parkes and Molonglo. The top panel shows the detection at Parkes, and the bottom panel shows the simultaneous detection at Molonglo. Note the different vertical scales for frequency.

dent discoveries (i.e. not in tandem with Parkes) of three FRBs by UTMOST (Caleb et al. 2017).

The MWA ( $\sim 600$  deg<sup>2</sup> field of view at 200 MHz) is also used, on occasion, to shadow SUPERB. Occasional shadowing has been performed since mid-2015 with more routine shadowing since 2016 January. Data are recorded using the standard mode of the MWA's hybrid correlator, recording visibilities at a cadence of 500 ms and 40 kHz. Furthermore, since the MWA's sensitivity is a strong function of zenith angle, in order to keep the loss in sensitivity minimal and ensure quality calibration, Parkes pointings that are west-most are preferentially selected while the MWA is available for shadowing (but see Section 5.4 for discussion of the RFI implications of this). The large field of view means there are no


**Figure 9.** The left-hand panel shows a Molonglo primary beam (green) at 843 MHz overlaid on the 13-beam sky footprint of Parkes (grey). Some Molonglo fan-beams are also shown. A simultaneous detection at both telescopes can thus be used for more precise localization than can be achieved at either telescope operating by itself. The right-hand panel shows a zoom-in on a single Parkes beam and shows three overlapping Molonglo fan-beams. Parkes FRBs are typically (although not always) in a single beam; Molonglo FRB detections are typically in one to three fan-beams. Combining this information an FRB can be localized an order of magnitude more precisely than with Parkes alone.



additional requirements in terms of additional calibration observations as multiple suitable sources are typically present for any given MWA pointing.

The 30-antenna GMRT is also used, on occasion, to shadow SUPERB, in particular in the 325-MHz band, where the 84 arcmin (FWHM) beam is well matched to Parkes as it fully encompasses all 13 beams of the multibeam receiver, albeit with non-uniform sensitivity. Simultaneously, detecting a potential low-frequency counterpart allows one to constrain both the spectral nature and scattering properties of any FRBs in addition to the ability to precisely localize it in the sky (at the level of a few arcseconds). Shadowing with GMRT is complex as one must consider the down time due to the difference in slew rates, the need for approximately hourly phase calibration observations. Data are recorded using the high-time resolution mode of the GMRT software correlator (Roy et al. 2010), whereby the visibilities are recorded once every 125 ms, at a spectral resolution of 65 kHz, over a bandwidth of 16.66 MHz, centred at a frequency of 325.83 MHz. Despite the inevitable temporal and dispersive smearing expected for any potential counterparts to the FRB signals, this still ensures good detection prospects; e.g. a putative low-frequency counterpart of FRB 110220 would be detectable as a  $7\sigma$  event. The time allocation and coordination considerations typically allow shadowing about 10 per cent of the SUPERB survey. The common visibility is ensured by preferentially going for northerly pointings ( $\delta > -40^\circ$ ) that are past transit for Parkes during the times the GMRT is used (again see Section 5.4).

#### 4.2 Triggering

When an FRB is found in the F Pipeline burst search, an alert is issued to the observers via email that can be visually inspected and assessed. If the signal is judged to be an FRB detection, a trigger is issued to collaborators for multiwavelength follow-up. SUPERB maintains agreements with a large number of telescopes and collaborations to search for the signatures of FRBs across the electromagnetic spectrum. At the highest energies, SUPERB triggers the High Energy Spectroscopic System (HESS; Bernl  hr et al. 2003) operating in the range 10 GeV to 10 TeV. At X-ray wavelengths the *Swift* satellite (Burrows et al. 2005) is triggered, which then observes X-ray photons from 0.2–10 keV.

Additionally, triggers are sent to the 2-m Liverpool telescope in La Palma, the 1.35-m Skymapper telescope in New South Wales, Australia, the 1-m Zadko telescope in Western Australia, the 2.4-m Thai telescope, the 8.2-m Subaru telescope in Hawaii and the 10-m Keck telescopes in Hawaii, the 6.5-m Magellan telescopes in Chile and the Blanco 4-m telescope in Chile using the Dark Energy Camera. At radio wavelengths, triggers are sent to the 64-m Sardinia radio telescope capable of observing at 1.4 GHz, the GMRT and the MWA (Tingay et al. 2013). Internally, the SUPERB collaboration also operates the Australia Telescope Compact Array (ATCA) to image the field of the FRB at 5.5 and 7.5 GHz. Follow-up timing of pulsar discoveries is also performed by some of the radio telescopes in this network.

#### 4.3 Multimessenger Searches

The SUPERB project has agreements in place with multimessenger facilities to search for counterparts to FRB events. A subset of FRB progenitor models involves merger events of compact objects and as such may have an associated gravitational wave counterpart. Furthermore, the redshift ranges for many of the FRBs are plausibly

within the relevant redshift horizon for ground-based gravitational wave detectors. As such we have an agreement in place with the LIGO consortium to identify counterparts in the Advanced LIGO data set. Some FRB progenitors may also exhibit a neutrino signal. Earth-based neutrino detectors, which are sensitive to muon interactions with neutrinos, use the Earth itself as a filter against background muon signals, essentially look through the planet. We have an agreement with the ANTARES collaboration (Ageron et al. 2011) to search for neutrino signals associated with FRBs.

#### 4.4 Public alerts

From 2018 April 01, SUPERB will issue public alerts of FRB discoveries, with an associated Astronomer’s Telegram. The alert will be in the VOEvent Standard in the FRB format currently being finalized. While at present Parkes is the dominant FRB search machine, having discovered 22 of the 31 FRBs known, it is envisioned that other instruments, in particular CHIME, ASKAP and MeerKAT, will soon contribute significantly to the known population. As such it makes sense to create and adopt a world standard for FRB follow-ups, and it is widely considered that public alerts are the best way to do this. The lead time to change to public alerts, as opposed to immediate adoption, is (a) to allow us to satisfy our commitments under agreements with partner instruments; and (b) allow finalization of the format for FRB VOEvents and development of associated tools, which is currently underway.

### 5 RESULTS

In this section, we describe the first results from the survey, including verification of the expected sensitivity, the impact of RFI on the survey, and discoveries of FRBs and pulsars.

#### 5.1 Survey sensitivity verification

To verify that the expected sensitivity of the survey is being achieved, we keep track of all of the detections of previously known pulsars, detected in the pipelines described above.

*Single-pulse search:* the sensitivity of the SUPERB survey to single pulses from pulsars was compared to the sensitivity from the HTRU survey (Burke-Spolaor et al. 2011a) for a subset of the detected pulsars. The theoretical flux density of a single pulse detected by the multibeam receiver is given by the modified radiometer equation:

$$S_{\text{peak}} = \frac{(S/N)T_{\text{sys}}\beta}{G\sqrt{n_p}\Delta\nu W}, \quad (3)$$

where  $S_{\text{peak}}$  is the peak flux density of the pulse,  $S/N$  is the signal-to-noise ratio as before,  $\beta$  is a correction factor to account for small losses due to the digitization ( $\beta \approx 1.066$  for 2-bit digitization in our case),  $G$  is the gain of the telescope beam,  $n_p$  is the number of polarizations summed to create the signal,  $\Delta\nu$  is the bandwidth and  $W$  is the pulse width. For a single pulse detected in the primary beam of the receiver with an  $S/N$  of 10 and a width of 1 ms, this corresponds to a peak flux density of 0.5 Jy. The sensitivity to single pulses was found to be unchanged between the SUPERB and HTRU surveys and consistent with flux densities expected from equation (3).

*Periodicity search:* we directly folded the survey data (up to and including 2015 February) using ephemerides of all-known pulsars that had a published mean flux density,  $S_{\text{mean}}$ , at 1400 MHz and whose position was observed at least once. After visually inspecting

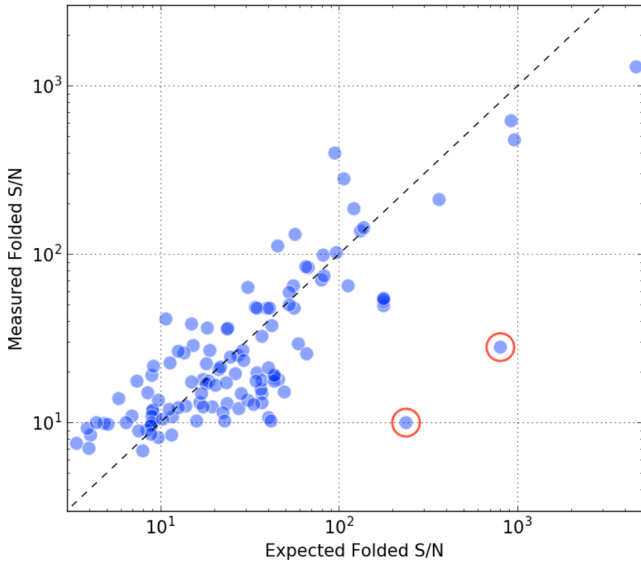


**Figure 11.** Measured versus expected folded S/N for known pulsars whose position was observed during the first part of the survey (excludes SUPERBx). The dashed line materializes the expected 1:1 correlation. Expected S/N has been computed under the assumption of a 5 per cent pulsar duty cycle. The outliers circled in orange correspond to two detections of J0904–7459, whose previously catalogued flux density at 1400 MHz appears to have been vastly larger than what our data indicate (see the text).

the output, we identified 124 detections of such pulsars and recorded their S/N. Using the modified radiometer equation appropriate for folded observations, one can compute the expected folded S/N of a pulsar with duty cycle  $\delta$ :

$$S/N = \frac{g S_{\text{mean}} G \sqrt{n_p} \Delta \nu T_{\text{obs}}}{\beta T_{\text{sys}}} \sqrt{\frac{1 - \delta}{\delta}}, \quad (4)$$

where  $T_{\text{obs}}$  is the integration time and  $g = \exp(-\alpha^2/2\alpha_0^2)$  is an adjustment to the boresight gain due to positional offset of the pulsar – the beam response is Gaussian;  $\alpha_0 = 6.0$  arcmin for the Parkes multibeam receiver. Fig. 11 displays the measured versus expected folded S/N for our sample of pulsars. The vast majority of sources follow the identity line as it should be. The only notable exception is PSR J0904–7459: it was seen twice with an S/N approximately 30 times lower than expected, and failed to be detected in two other observations where it should have been seen with S/N  $\approx 150$ . These repeated and consistent discrepancies suggest that the catalogued flux density of B0904–74 (J0904–7459) is erroneously high, an inference that is supported by a recent large-scale study of pulsar spectral properties (Jankowski et al. 2017). As a result of this realization, the pulsar catalogue (version 1.56) has now been updated to reflect our observations (R.N. Manchester, private communication).

We also checked which known pulsars of our sample were not properly detected by our search pipeline. The notable non-detections of PEASOUP are listed in Table 4. None of those are surprising as they can be explained by either the presence of RFI, or the fact that the FFT tends to lose sensitivity to signals with long periods. SPINN gave a score lower than 0.5 only to a single pulsar observation, whose candidate plot was heavily affected by impulsive RFI. This can also be seen in Fig. 8, where the false negative rate at a score of 0.5 is not quite zero.

**Table 4.** List of notable non-detections of PEASOUP. We also ran the SEEK routine of the well-established SIGPROC pulsar searching package, and obtained three faint detections. No major discrepancy can be seen though. One can also note the potential benefits of an FFA-based pulsar search. Note that J1910+0714 was affected by impulsive RFI, and J1105–4357 was impacted by the presence of periodic RFI at a period of 1000.0 ms.

Name	$P$ (ms)	DM	Folded S/N	SEEK S/N
J1105–4357	351.1	38.3	12.2	6.9
J1842+0257	3088.3	148.1	13.9	6.7
J0633–2015	3253.2	90.7	14.0	–
J0636–4549	1984.6	26.3	14.0	–
J1846–7403	4878.8	97.0	14.1	6.4
J1910+0714	2712.4	124.1	17.6	–
J1945–0040	1045.6	59.7	24.6	–

## 5.2 FRBs

The first FRB discovered by SUPERB is FRB 150418. This source has been reported in Keane et al. (2016) and further discussed in many subsequent publications as we now recap. FRB 150418 is at low Galactic latitude ( $b = -3.3^\circ$ ) but despite this is clearly extragalactic with DM/DM<sub>Milky Way</sub> of 4.2 (2.4) according to the NE2001 (YMW16) model of the electron density in the Galaxy (Cordes & Lazio 2002; Yao, Manchester & Wang 2017). In brief, the main point of subsequent discussion has been the statistical association (and its implications) discussed in Keane et al. (2016). This association, with a source in the elliptical galaxy WISE J071634.59–190039.2, was based on its contemporaneous brightening and an estimate of the likelihood of its light curve ( $\sim 99$  per cent probability of association, based on five observation epochs). Further observations at the highest angular resolutions show that the source (which must be more compact than  $\sim 10$  pc) is most likely an AGN (Bassa et al. 2016; Giroletti et al. 2016). As more data became available, the light curve of the variable radio source became ever better characterized and the statistical significance of the association reduced (to  $\sim 92$  per cent, based on 24 epochs, see e.g. Williams & Berger 2016; Johnston et al. 2017). Unless a repeat FRB is seen from the source, this association is thus likely to remain somewhat controversial, at least until such time as the statistics of longer ( $\sim$ day) time-scale variability at below 100  $\mu$ Jy becomes clearer.

Four further FRB discoveries from SUPERB will be reported in detail, along with their multiwavelength and multimessenger follow-up, in Paper II in this series.

## 5.3 New pulsars

The first 10 pulsars discovered in this survey are listed in Table 5. For seven of these, the positions listed denote the phase centre of the beam in which they were discovered and should only be taken as indicative prior to a full timing solution being obtained; the exceptions are identified below. Fig. 12 shows the pulse profiles.

**PSR J0621–55:** this source was found in the single-pulse pipeline and is undetectable in our periodicity searches. As such it can be classified as a ‘RRAT’ (Keane & McLaughlin 2011). As only three pulses have been detected for this source, it has not yet been possible to identify any underlying periodicity.

**PSR J0749–68:** this pulsar is undetected in several observations but has high S/N in others; its period-averaged flux density is 4.1 mJy. This may be due to scintillation or possibly nulling. The profile is broad with a width of  $80^\circ$ . It has a 40 per cent linear polarization fraction that is high given the pulsar’s long spin period.



**Table 5.** The parameters of 10 newly discovered pulsars from the SUPERB survey. The timing solution for PSR J1421–4409 is detailed in Table 6. We list the positions in both equatorial coordinates with uncertainties and the equivalent Galactic coordinates omitting those same uncertainties, the spin period ( $P$ ), the DM and the NE2001-derived distances of these pulsars. Values in parentheses are the nominal  $1\sigma$  uncertainties in the last digits. We understand that two of these pulsars have been independently identified, but not yet published, in two other ongoing surveys denoted here as \* = GBNCC and \*\* = PALFA.

PSR name	R.A. (J2000) (h:m:s)	Dec. (J2000) (°:′:″)	$l$ (°)	$b$ (°)	$P$ (ms)	DM (cm <sup>−3</sup> pc)	Dist (kpc)	Comment
J0621–55	06:20.7(5)	−56:05(7)	264.822	−26.416	–	22	1.1	RRAT
J0749–68	07:50:50(1)	−68:44:27(4)	281.013	−20.110	915.171 299(2)	26	1.1	scintillates
J1126–38*	11:26.3(5)	−38:38(7)	285.230	21.286	887.55(1)	46	1.7	
J1306–40	13:06:56.0(5)	−40:35:23(7)	306.108	22.186	2.204 53(2)	35	1.2	MSP, intermittent
J1337–44	13:37.1(5)	−44:43(7)	311.412	17.386	1257.52(9)	96	3.5	Nuller
J1405–42	14:05.8(5)	−42:33(7)	317.249	18.233	2346.80(4)	64	2.0	–
J1421–4409	14:21:20.9646(3)	−44:09:04.541(4)	319.497	15.809	6.385 728 838 16(3)	54.6	1.6	MSP, binary
J1604–31	16:04.4(5)	−31:39(7)	344.118	15.380	883.883(5)	63	1.9	–
J1914+08**	19:14.3(5)	−08:45(7)	43.327	−1.042	440.048(2)	285	7.0	–
J2154–28	21:54.8(5)	−28:08(7)	20.854	−51.089	1343.35(2)	28	1.2	–

**Table 6.** Ephemerides for PSR J1421–4409.

Parameter	Value (Error)
Epoch (MJD)	57 600
Pulse period, $P$ (ms)	6.385 728 838 16(3)
Period derivative, $\dot{P}$ (10 <sup>−20</sup> )	1.27(4)
Right ascension, $\alpha$ (J2000.0)	14 <sup>h</sup> 21 <sup>m</sup> 20 <sup>s</sup> .9646(3)
Declination, $\delta$ (J2000.0)	−44°09′04″.541(4)
$\mu_\alpha$ (mas yr <sup>−1</sup> )	−10(8)
$\mu_\delta$ (mas yr <sup>−1</sup> )	3(2)
Composite proper motion, $\mu$ (mas yr <sup>−1</sup> )	11(8)
Celestial position angle, $\phi_\mu$ (°)	−70(2)
Dispersion measure, DM (pc cm <sup>−3</sup> )	54.635(4)
Binary model	ELL1
Solar system ephemeris	DE421
Orbital period, $P_b$ (d)	30.746 4535(2)
Projected semi-major axis, $x$ (lt-s)	12.706 655(5)
Orbital eccentricity, $e$	0.000 0128(4)
Epoch of periastron, $T_0$ (MJD)	56 935.6(1)
Longitude of periastron, $\omega$ (°)	39(1)
Mass function ( $M_\odot$ )	0.002 330(8)
Characteristic age, $\tau_c$ (Gyr)	7.97

Circular polarization is modest and shows a change in sign close to the profile peak (see Fig. 13). We measure the rotation measure to be  $-23 \pm 2$  rad m<sup>−2</sup>. The position angle (PA) swing is relatively flat leading to the conclusion that the pulsar is an almost aligned rotator. A partial timing solution has been obtained for this pulsar so that, as indicated in Table 5, its position is determined more accurately than most of the sources presented here.

**PSR J1126–38:** this 887-ms pulsar, although not previously reported, appears to have also been independently discovered<sup>5</sup> by the Green Bank North Celestial Cap (GBNCC) survey.

**PSR J1337–44:** this slow pulsar appears to be nulling and as such is difficult to time, at least at  $\sim 1.4$  GHz. Our efforts to observe this source at  $\sim 750$  MHz at Parkes (pulsars generally being stronger at these lower frequencies; Bates, Lorimer & Verbiest 2013) have been scuppered due to the recent appearance of strong terrestrial RFI in the band. The origin of this RFI is a 4G telephone based station now located less than 10 km from the telescope. Given this and the southerly declination of the source, it may evade a full timing

solution for a while. The nulling seems to be intrinsic as scintillation might be precluded as the pulsar’s DM implies a scintillation bandwidth that is much smaller than our observing bandwidth.

**PSR J1405–42:** this 2.3-s pulsar is the slowest in our sample. It would have been missed were it not for our RFI mitigation techniques. We expect our final pulsar sample to contain a much higher fraction of such slow pulsars as we focus efforts on relevant RFI mitigation strategies as well as optimized searching, e.g. with the FFA pipeline.

**PSR J1604–31:** in contrast to PSR J0749–68, the profile is very narrow with a width of only 5°. The fractional polarization is low and no RM is measurable.

**PSR J1914+08:** this 440-ms pulsar is the one with by far the highest DM in our sample, as one might expect for the source that is closest to the Galactic plane. Although not previously reported, it appears to have also been independently discovered<sup>6</sup> by the Pulsar Arecibo L-band Feed Array (PALFA) survey.

**PSR J2154–28:** this pulsar was initially missed in the F pipeline but was detected in the T pipeline as a result of the additional RFI mitigation performed therein.

### 5.3.1 PSR J1306–40

This pulsar has a period of 2.2 ms and has proven to be the most elusive of those reported here. It was initially detected in 2015 June in two survey pointings separated by 30 min (see Fig. 14). The S/N of these initial two detections were  $\sim 14$  and  $\sim 23$ . The source then proved undetectable in extended efforts to re-detect it in a total observation time of 9 h. Combining the two detections, we derived an improved sky position for the source ‘in between’ the two survey pointings, by considering the beam model and weighting appropriately by the S/N values. Focusing on this refined position, our best estimate for the true position, we later re-detected the source twice again in 2016 September in observations 5 d apart. In each detection, the signal is seen with a positive orbital acceleration where the convention is such that this implies we are observing the pulsar on the ‘near’ side of its orbit. Although four detections is a small sample this is suggestive of an eclipsing system where the pulsar is not detectable when on the ‘far’ side of the orbit. The difficulty in detecting this source is also likely compounded by scintillation. The nominal sky position of the pulsar also happens to be within

<sup>5</sup> As inferred from the survey’s web pages: <http://astro.phys.wvu.edu/GBNCC/>.

<sup>6</sup> As inferred from the survey’s web pages: <http://www.naic.edu/palfa>.

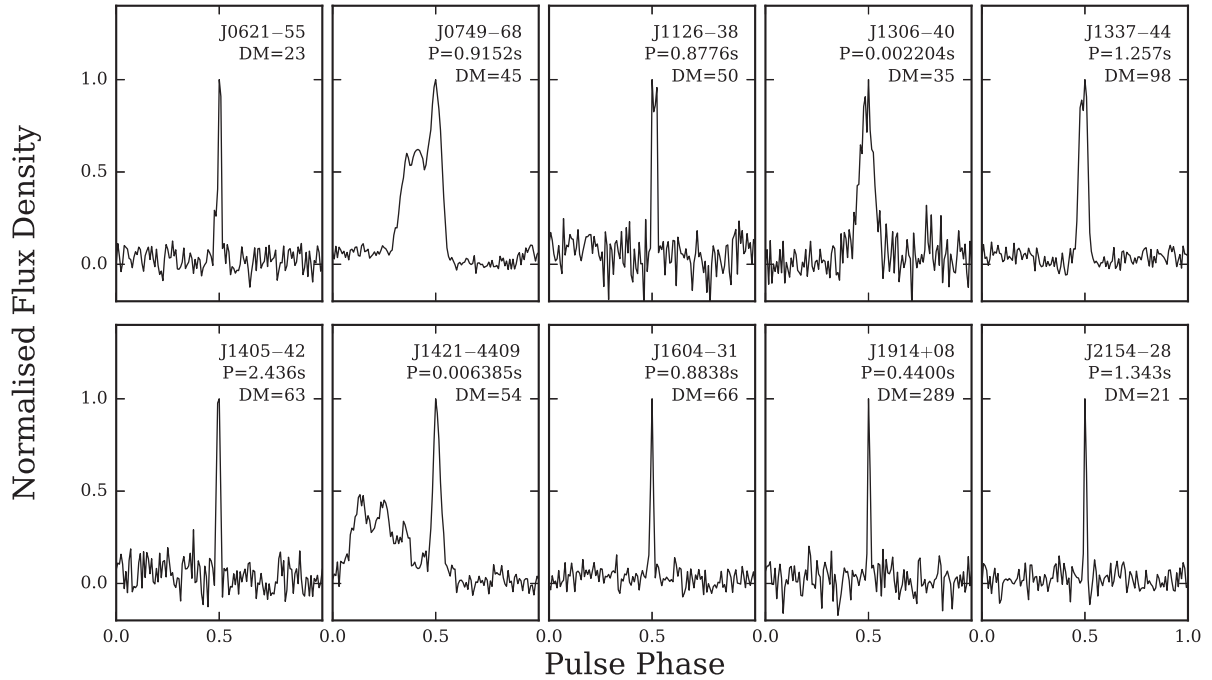


**Figure 12.** Pulse profiles of the first 10 pulsar discoveries from SUPERB. Each panel shows one pulse period and the pulsar name is given in the top right corner, along with its rotation period in seconds and DM in units of  $\text{cm}^{-3} \text{pc}$ . J0621–55 does not yet have a determined periodicity.

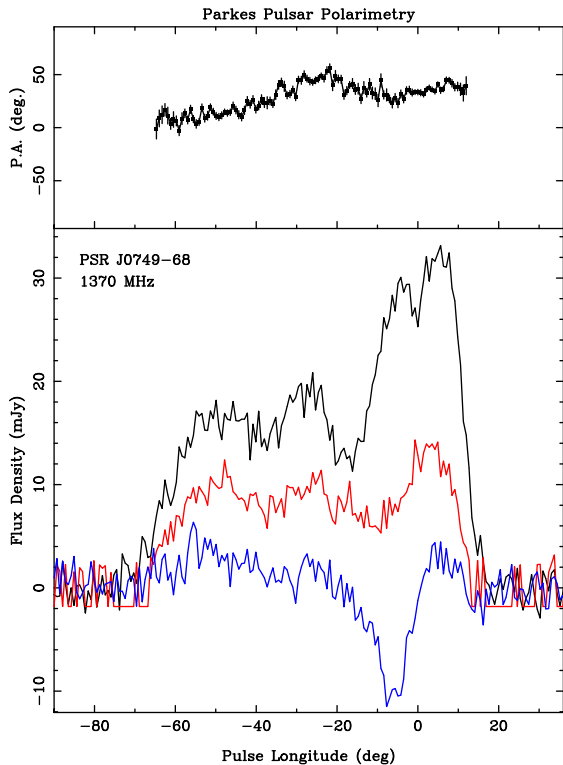


**Figure 13.** Polarization properties of PSR J0749–68. In the upper panel, the polarization PA is shown. In the lower panel black, blue and red denote total intensity, linear and circular polarization, respectively.

the field where there are 130 ks of observation accumulated, by XMM Newton, as part of a study of a nearby Seyfert galaxy. In these data, it can be seen that the nominal position of the pulsar is coincident with the source 3XMM J130656.2–403523. The

spectrum of the source is at first glance consistent with what one might see in an eclipsing ‘red back’ binary system, with a hint of variability on a  $\sim 1/2$ -d time-scale, but it is unclear if the spectrum is reliable given the source’s location so close to the edge of the detector.

Linares (2017) has further studied these X-ray data, along with optical data from the Catalina Sky Survey, and derives a period of 26.3 h. Extrapolating this period to the times at which our radio detections have been made shows that our detections are indeed all on the ‘near’ side of the orbit, but with several non-detections also falling in this range. These non-detections might be attributable to scintillation or ‘transitional’ behaviour in the system. Overall the picture is consistent with the red back hypothesis. We will report in further detail on our ongoing studies of this source in future publications.

### 5.3.2 PSR J1421–4409

Discovered in the real-time periodicity search pipeline, PSR J1421–4409 (hereon J1421) is the first millisecond pulsar discovered by SUPERB. Its pulse profile is complex as seen in many MSPs, e.g. Dai et al (2015) with half-maximum width of just  $11^\circ 2$  but, because of the trailing peak, reaches the 10 per cent level only after  $176^\circ$  of pulse phase. The pulse-averaged flux density is 1.4 mJy and the linear polarization is low, at just 10 per cent (see Fig. 15). We estimate the rotation measure to be  $-43 \pm 8 \text{ rad m}^2$ . The linear polarization loosely tracks the total intensity profile but the circularly polarized component becomes significant in the trailing half of the profile, presenting a change in handedness from right to left. Individual observations were polarization calibrated following the Measurement Equation Template Matching technique described in van Straten (2013) to correct for the cross-coupling of the feeds, using long-track observations of PSR J0437–4715. Additionally, the gain imbalance between the receiver feeds was corrected by

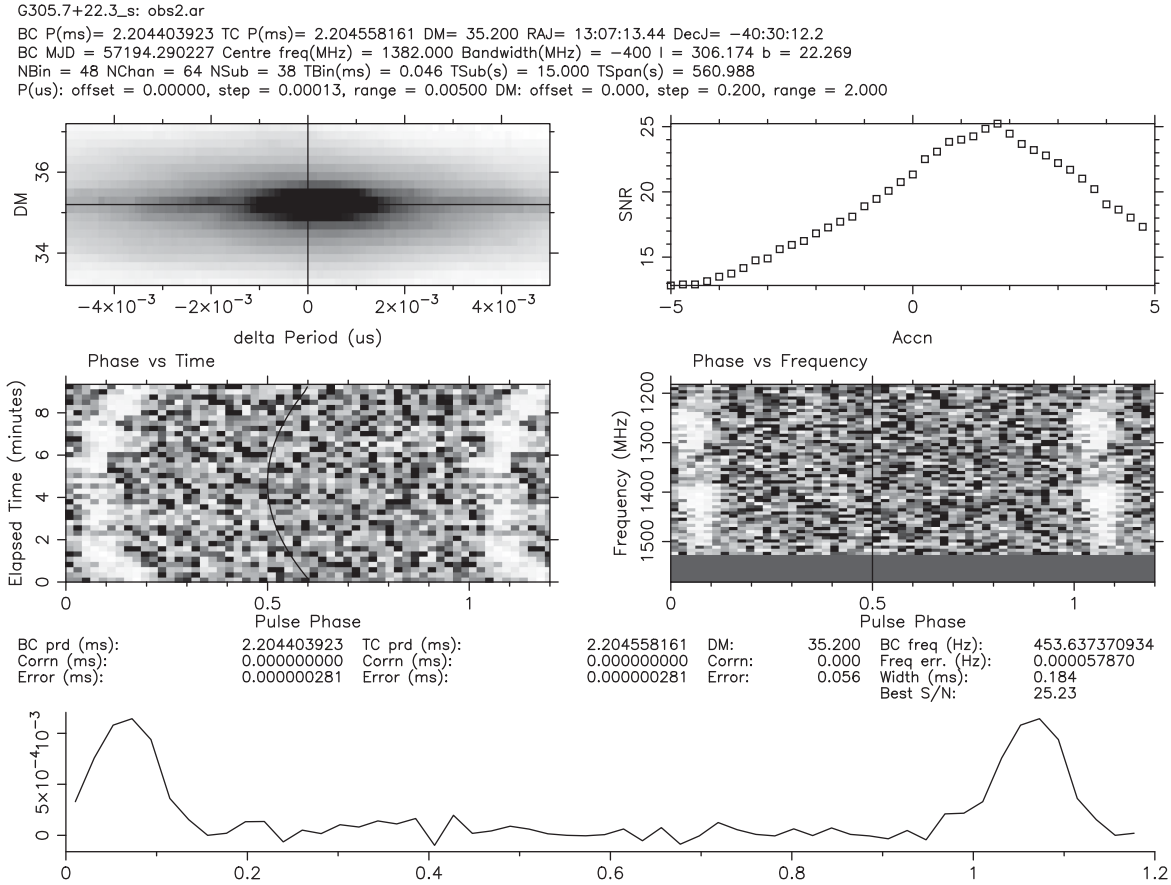


**Figure 14.** One of the detections of PSR J1306–40. The top left panel shows the S/N (in grey-scale) as a function of trial DM and period; the top right panel shows the S/N as a function of trial acceleration – a highly significant orbital acceleration is evident. The middle panels show the S/N (grey-scale) as a function of time during the observation (left) and frequency across the observing band (right). The bottom panel shows the integrated pulse profile at the optimized period, acceleration and DM.

utilizing square wave observations of a noise diode with known polarization properties.

The pulsar has a 6.3-ms spin period and resides in a 30.7-d binary system. With a minimum companion of mass of  $0.18 M_{\odot}$ , J1421 would appear to be a typical PSR-HeWD binary. However, binary periods between 22 and 48 d are rare for MSPs (the ‘Camilo gap’; Camilo 1995) with the only Galactic-field PSR-HeWD binaries known to have orbital periods in this range being the so-called eccentric MSPs (eMSPs; Barr et al. 2017). Although several have been proposed, there is currently no generally accepted model describing the evolution of eMSPs. One model of note for discussion of J1421 is that of Antoniadis (2014). In this model, hydrogen shell flashes at the end of the recycling phase result in a super-Eddington mass transfer rate between the donor and companion. Matter then cannot be accreted on to the neutron star and forms a circumbinary disc and it is through interaction with this disc that eccentricity is induced in the system. Antoniadis (2014) predicts that non-eccentric binaries can also exist in this gap if they are capable of photoevaporating their circumbinary discs before they can induce eccentricity in the orbit. A pulsar’s capability to photoevaporate its disc is proportional to its spin-down luminosity and inversely proportional to its semi-major axis distance. If we compare J1421’s properties to those of the eMSPs, we find that it has a slightly lower projected semimajor axis distance than the eMSPs (12.7 lt-s as compared to a median of 14 lt-s for the eMSPs) and its spin-down luminosity is close to the mean of the eMSPs,  $4.6 \times 10^{33}$  erg s $^{-1}$ . As such J1421 does not clearly

distinguish itself from the eMSPs and thus presents a challenge to the circumbinary disc model.

As shown in Fig. 16, J1421 falls in the previous identified gap in eccentricity–binary period space, and is indeed more similar to the ordinary PSR-HeWD binaries. For orbital periods larger than 2 d, their evolution is usually well understood, allowing one to derive an orbital period–companion mass relationship (Tauris & Savonije 1999), which appears to describe the known systems well. Assuming its validity also for J1421, the companion mass should be  $\sim 0.28 M_{\odot}$ . This relatively large value would imply a relatively low orbital inclination angle given the value of the mass function. Assuming a range of pulsar masses between  $1.2$  and  $1.7 M_{\odot}$ , the implied inclination angle ranges between  $38^{\circ}$  and  $48^{\circ}$ , respectively. One can try to constrain the orbital inclination angle also from the polarization properties of the pulse profile. If the pulsar’s PA swing can be described by a rotating vector model (RVM; Radakrishnan & Cooke 1969), the viewing angle between the spin axis and the line of sight to the observer at the closest approach to the magnetic axis,  $\zeta$ , should be similar to the orbital inclination angle  $\zeta \sim i$ , if the recycling process spinning up J1421 to its current period led to the expected alignment of orbital angular momentum and spin axis. However, fitting RVMs to recycled pulsars is often difficult, although recent results (e.g. Freire et al. 2017; Berezhina et al. 2017) suggest that it is possible in an increasing number of cases. We fitted the RVM to the PA data of J1421 (see Fig. 15). We use the PSR/IEEE convention as explained in detail in van Straten,

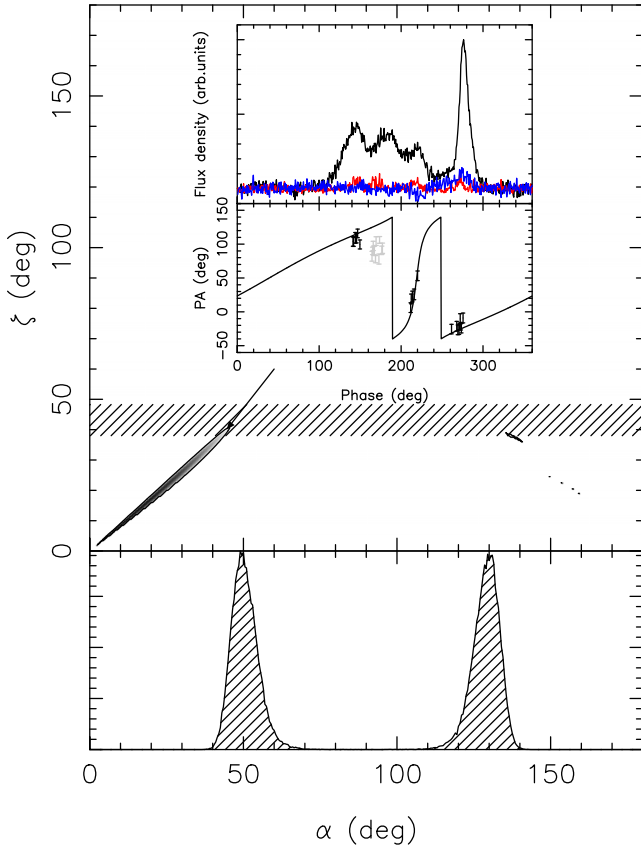


**Figure 15.** Polarization properties of PSR J1421–4409. The main top panel shows the system geometry as derived from a least-squares fit of the RVM to the PA of the linearly polarized emission; also shown are regions of the magnetic inclination angle ( $\alpha$ ) and viewing angle ( $\zeta$ ) plane with the best RVM fits ( $1\sigma$  contours). We also mark the constraint on the orbital inclination angle as a horizontal strip. Also, assuming a filled emission beam, we derive a distribution of inclination angles (lower panel) that is consistent with the observed pulse width. For the point that satisfies the profile, polarimetric and orbital inclination constraints ( $\alpha = 44^\circ$  and  $\zeta = 40^\circ$ ), we calculate the RVM PA versus phase curve and superimpose it on the measurements (bottom panel of inset). The top inset panel shows the pulse profile using the same conventions as in Fig. 13.

Manchester Johnston & Reynolds (2010), minimizing  $\chi^2$  for a combination of  $\zeta$  and the magnetic inclination angle  $\alpha$ . The resulting  $1\sigma$  contours are shown in Fig. 15. The best solution implies small  $\alpha$  and  $\zeta$  values. This is consistent with a wide pulse profile, as observed. However, the data are consistent also with values as large as  $\sim 45^\circ$ . One solution is shown as a solid line in the PA-pulse phase plot below the pulse profile shown in the inset, representing a so-called inner line of sight (e.g. Lorimer & Kramer 2005). The data points in light grey have been ignored during the fit and are shown here shifted by  $90^\circ$  (an orthogonal jump) from their original value. Non-orthogonal jumps are not uncommon, but given the low level of the associated linear polarization they were excluded. Including these data points in the fit does not change the best-fitting solution but increases the size of the contours.

The RVM solution corresponds to a combination of angles indicated by the arrow ( $\alpha \sim 44^\circ$ ,  $\zeta \sim 40^\circ$ ). The solution was chosen as an example for the following reasons. Assuming that the open field-line region of the pulsar is filled with emission, the observed pulse width can be related to  $\alpha$  and  $\zeta$  and the angular radius of the open

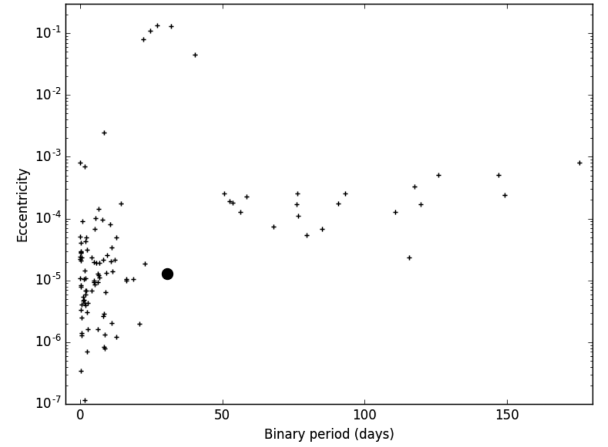


**Figure 16.** Eccentricity and binary period for every binary MSP that is not in a double neutron star system, globular cluster and does not have a main-sequence companion. PSR J1421–4409 is identified with a large black circle. It can be seen that its eccentricity is anomalously low for systems in this period range, the so-called Camilo gap.

field line region,  $\rho$ . There are indications that this assumption is often not fulfilled for recycled pulsars (Kramer et al. 1998), but it can serve as a useful guide (e.g. Freire et al. 2017). Assuming a period- $\rho$  scaling as found for normal pulsars (e.g. Kramer et al. 1994), we performed Monte Carlo simulations that result in a distribution of  $\alpha$  values consistent with the observed pulse width (see Berezhina et al. 2017, for details). Under these assumptions, two ranges of  $\alpha$  values are consistent with the data, centred on  $50^\circ$  and  $130^\circ$ , respectively, as shown in the distribution below the  $\alpha$ - $\zeta$  plane. Moreover, we can also indicate the range of inclination angles as derived from the Tauris–Savonije relationship, assuming that  $\zeta \sim i$ . The corresponding range is indicated by the horizontal hashed region. As shown by the arrow, we can find a solution that is consistent with the data and the described constraints. While this is not a unique solution, it does provide a consistent picture of the evolution of the system, the pulse profile and the polarization information.

#### 5.4 Radio frequency interference

The survey has been subject to a large amount of RFI. This comes in many forms – external sources (e.g. satellites, air traffic control radar, malfunctioning observatory equipment) and internal sources (e.g. self-induced RFI in individual beams, due to maintenance issues with the multibeam receiver). RFI is time variable on a number of scales and can be both narrow and broad-band. Generally speaking at Parkes, as with most observatories worldwide, the RFI environment is getting worse over time; even the Murchison Radio Observatory site, perhaps the best radio astronomy site on the planet is subject to these effects (Sokolowski, Wayth & Morgan 2015). These effects have a strong deleterious effect on our ability to detect astrophysical signals. We are attempting to perform a census of the RFI environment at Parkes using the SUPERB data set. By characterizing the RFI as fully as possible, we can improve the quality of our data and thus identify otherwise obscured astrophysical signals (we have had success with this already – see above); this information should be useful to all other users of the observatory also. Here, as an initial illustration of this work, we present several metrics to quantify the effects of RFI in our data. We examine (i) the number of time-samples removed by our RFI cleaning algorithms

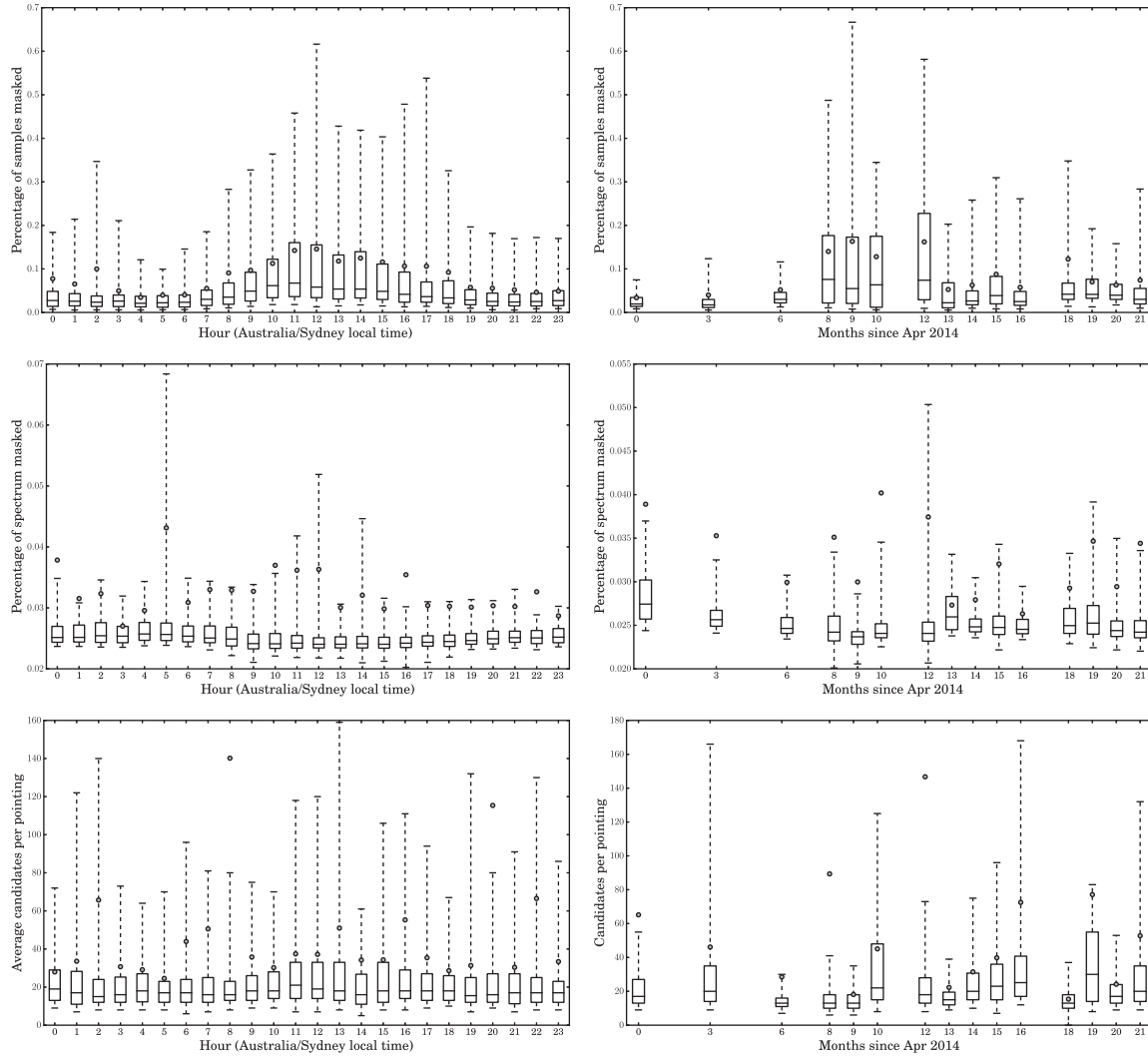


**Figure 17.** Illustrations of three assessments of the RFI environment at Parkes, as a function of time, during the survey observations reported here. The metrics are shown on hourly (left) and monthly (right) time-scales. Top row: the percentage of time samples masked in the eigenvector decomposition-based assessment. Middle row: the percentage of spectral bins masked in the ‘birdie’ search. Bottom row: the number of detected single pulse events above a threshold (more than six times the standard deviation in excess of the mean) in each pointing. These metrics are derived from a representative sample of 10 000 random survey pointings.

after an eigenvalue decomposition of the input from all 13 beams – this affects both periodicity and single-pulse searches; (ii) the number of ‘birdies’, i.e. frequencies in the fluctuation spectra that were removed by our algorithms – this affects the periodicity searches; (iii) the number of single-pulse candidates generated – this clearly is only a metric relevant to single-pulse searches. The criteria used for identifying these signals are threshold searches by comparison with the expectation of white noise – in the case of the birdie search, an initially ‘de-reddening’ of the fluctuation is performed. These metrics are illustrated in Figs 17 and 18 where we examine altitude and azimuth dependence of these quantities, and their time variability on hourly and monthly time-scales. Several patterns are evident in the data, e.g. that RFI is more prevalent during local working hours and contamination is worst for westerly pointings. A thorough examination of the wide range of RFI signals in the data will be presented in a later paper.

## 6 SUMMARY

We have presented the features of SUPERB, an experiment designed for searching for pulsars and fast transients using the multi-beam receiver of the Parkes radio telescope in the 1400-MHz band. The survey exploits a usable bandwidth of  $\sim 340$  MHz, split into 390 kHz wide channels; the integration time is 9 min and the voltages are sampled at 2 bits every 64  $\mu$ s. In the observations reported here covering the time up to and including 2016 January have accumulated an observing time-field of view product of  $\sim 1350$  deg h (to the half-power sensitivity level), and have tessellated most of the sky visible from Parkes, with particular focus on the intermediate and high Galactic latitudes.

SUPERB has introduced a few significant improvements with respect to the past large-scale surveys for pulsar and/or transients carried on at Parkes or elsewhere: (i) the implementation of a



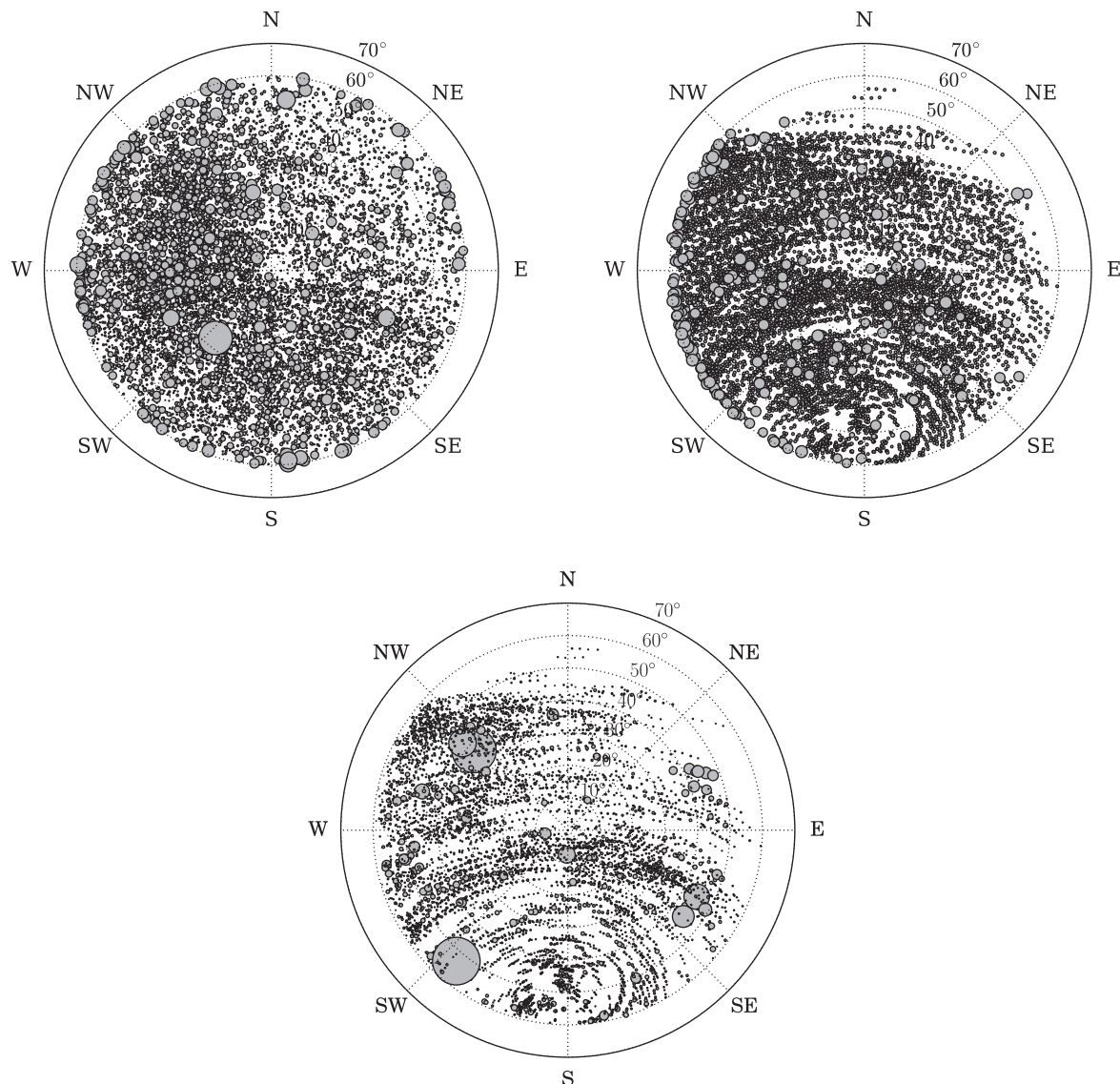


**Figure 18.** Illustrations of three assessments of the RFI environment at Parkes, as a function of azimuth and zenith for the survey observations reported here. The quantities plotted are the same as in Fig. 17: percentage masked samples in the top two panels (time samples on the left, frequencies on the right), and number of excess single pulse candidates in the bottom panel. In each panel, the centre of each circle is at the position of the single pointing in question and the area of the circle denotes the magnitude of the quantity. Again, these metrics are derived from a random representative sample of 10 000 survey pointings.

real-time search for both periodic (both isolated and binary systems) and transient signals, followed by an offline deeper analysis of all the collected data; (ii) the capability of quickly distributing alerts for the occurrence of transient signals and the associated triggering of a multimessenger campaign for follow-ups of the transient signals; (iii) the set-up of a program of observations shadowing the survey pointings; (iv) the availability of full-Stokes data for transients. Observations are in agreement with the expected limiting sensitivity of the surveys.

Here, we have reported on the first 10 pulsar discoveries. One of the two new millisecond pulsars, PSR J1421–4407 (6.4 ms spin period) is in a 30.7-d orbit, showing a remarkably small eccentricity in comparison with the other already known systems with a similar orbital period. PSR J1306–40 is a 2.2-ms pulsar in an orbit that is as

yet unsolved. Indications are that it may be eclipsed by its companion (or associated winds) for a significant fraction of its orbit, and may be similar to the red back binary systems. Further pulsar discoveries, with a particular focus on new ultralong period pulsars, will be reported in subsequent papers in this series. The next four FRB discoveries (joining the already reported FRB 150418) will be reported in [Paper II](#). The number of discoveries is roughly in agreement with the expectations based on simple pulsar population models. This will be examined in detail in the future using the SUPERB data set to include intermittency, scintillation etc. into pulsar population modelling for the first time. SUPERB looks set to continue working successfully and will continue to adapt and improve over time. For example, as new computing capabilities become available and new telescope equipment, such as cooled phased array feeds, come into

use, the parameter space searched opens up and the survey gets ever better.

## DATA ACCESS

Data obtained in this project are archived for long-term storage on the CASS/ANDS data server. These data are publicly available 18 months from the day they are recorded. The data are recorded in SIGPROC filterbank format, a *de facto* standard for pulsar search data, and are converted to PSRFITS format for upload to the data server<sup>7</sup>. From here they can be accessed by anybody. The full resolution data products are produced at a rate of  $\sim 46$  MiB/s when observing. For typical observing efficiencies (considering telescope stowing due to wind, RFI or maintenance issues that occur during routine observing) this amounts to  $\sim 4$  TB per day of observation.

## ACKNOWLEDGEMENTS

The SUPERB collaboration would like to thank S. D. Bates and D. J. Champion for performing observations for the survey, as well as the whole team of support staff at Parkes, and in Marsfield, for their continuing sterling efforts essential to the success of all of the programmes running at the facility. The Parkes radio telescope is part of the Australia Telescope National Facility which is funded by the Commonwealth of Australia for operation as a National Facility managed by CSIRO. Parts of this research were conducted by the Australian Research Council Centre of Excellence for All-sky Astrophysics (CAASTRO), through project number CE110001020. This work was performed on the gSTAR national facility at Swinburne University of Technology. gSTAR is funded by Swinburne and the Australian Government's Education Investment Fund. EP receives funding from the European Research Council under the European Union's Seventh Framework Programme (FP/2007-2013)/ERC Grant Agreement no. 617199. The work of MK and RPE is supported by the ERC Synergy Grant 'BlackHoleCam: Imaging the Event Horizon of Black Holes' (Grant 610058).

## REFERENCES

- Ageron M. et al., 2003, *Nucl. Instrum. Methods Phys. Res. A*, 656, 11  
 Antoniadis J., 2014, *ApJ*, 797, L24  
 Bailes M. et al., 2011, *Science*, 333, 1717  
 Bannister K. W., Stevens J., Tuntsov A. V., Walker M. A., Johnston S., Reynolds C., Bignall H., 2016, *Science*, 351, 354  
 Barr E. D. et al., 2017, *MNRAS*, 465, 1711  
 Barsdell B. R., Barnes D. G., Fluke C. J., 2010, *MNRAS*, 408, 1936  
 Bassa C. G., Freire P. C. C., Kramer M., Champion D. J., Berezina M., Bassa C. G., Lyne A. G., Stappers B. W., 2016, *MNRAS*, 463, L36  
 Bates S. D., Lorimer D. R., Verbiest J. P. W., 2013, *MNRAS*, 431, 1352  
 Berezina M. et al., 2017, *MNRAS*, 470, 4421  
 Bernlöhr K. et al., 2003, *Astropart. Phys.*, 20, 111  
 Bhandari S. et al., 2017, *MNRAS*, in press (Paper II)  
 Braun R., Bourke T., Green J. A., Keane E., Wagg J., 2015, *Proc. Sci., Advancing Astrophysics with the Square Kilometre Array (AASKA14)*. SISSA, Trieste, PoS#174  
 Burke-Spolaor S. et al., 2011a, *MNRAS*, 416, 2465  
 Burke-Spolaor S., Bailes M., Ekers R., Macquart J.-P., Crawford F., III, 2011b, *ApJ*, 727, 18  
 Burrows D. N. et al., 2005, *Space Sci. Rev.*, 120, 165  
 Caleb M. et al., 2017, *MNRAS*, 468, 3746  
 Cameron A. D., Barr E. D., Champion D. J., Kramer M., Zhu W. W., 2017, *MNRAS*, 468, 1994  
 Camilo F., in Alpar A., Kiziloglu U., van Paradis J. eds, *The Lives of the Neutron Stars*. Kluwer, Dordrecht, p. 243  
 Cordes Lazio, 2002, preprint ([astro-ph/0207156](https://arxiv.org/abs/astro-ph/0207156))  
 Deng X. et al., 2017, *PASA*, 34, 26  
 Freire P. C. et al., 2017, *MNRAS*, 471, 857  
 Giroletti M., Marcote B., Garrett M. A., Paragi Z., Yang J., Hada K., Muxlow T. W. B., Cheung C. C., 2016, *A&A*, 593, L16  
 Hallinan G. et al., 2007, *ApJ*, 663, L25  
 Horesh A., Cenko S. B., Perley D. A., Kulkarni S. R., Hallinan G., Bellm E., 2015, *ApJ*, 812, 86  
 Hotan A. W., van Straten W., Manchester R. N., 2004, *PASA*, 21, 302  
 Hyman S. D., Lazio T. J. W., Kassim N. E., Ray P. S., Markwardt C. B., Yusef-Zadeh F., 2005, *Nature*, 434, 50  
 Jankowski F. et al., 2017, *MNRAS*, in press  
 Johnston S. et al., 2017, *MNRAS*, 465, 2143  
 Keane E. F., 2016, *MNRAS*, 459, 1360  
 Keane E. F., McLaughlin M. A., 2011, *Bull. Astron. Soc. India*, 39, 333  
 Keane E. F. et al., 2016, *Nature*, 530, 453  
 Keith M. J. et al., 2010, *MNRAS*, 409, 619  
 Keith M. J. et al., 2011, *MNRAS*, 419, 1752  
 Kocz J., Briggs F. H., Reynolds J., 2010, *AJ*, 140, 2086  
 Kondratiev V. I., McLaughlin M. A., Lorimer D. R., Burgay M., Possenti A., Turolla R., Popov S. B., Zane S., 2009, *ApJ*, 702, 692  
 Kramer M., Stappers B. W., 2015, *Proc. Sci., Pulsar Science with the SKA*. SISSA, Trieste, PoS#36  
 Kramer M., Wielebinski R., Jessner A., Gil J. A., Seiradakis J. H., 1994, *A&AS*, 107, 515  
 Kramer M., Xilouris K. M., Lorimer D. R., Doroshenko O., Jessner A., Wielebinski R., Wolszczan A., Camilo F., 1998, *ApJ*, 501, 270  
 Kramer M., Lyne A. G., O'Brien J. T., Jordan C. A., Lorimer D. R., 2006, *Science*, 312, 549  
 Leshem A., van der Veen A.-J., 2000, in Smolders A., Haarlem M., eds, *Introduction to Interference Mitigation Techniques in Radio Astronomy Perspectives on Radio Astronomy: Technologies for Large Antenna Arrays*. ASTRON, Dwingeloo, p. 201  
 Levin L. et al., 2010, *ApJ*, 721, L33  
 Levin L. et al., 2013, *MNRAS*, 434, 1387  
 Linares M., 2017, *MNRAS*, preprint ([astro-ph/1707.00698](https://arxiv.org/abs/astro-ph/1707.00698))  
 Lorimer D. R., Kramer M., 2005, *Handbook of Pulsar Astronomy*. Cambridge Univ. Press, Cambridge  
 Lorimer D. R., Bailes M., McLaughlin M. A., Narkevic D. J., Crawford F., 2007, *Science*, 318, 777  
 Lyne A. G., Johnston S., Manchester R. N., Staveley-Smith L., D'Amico N., 1990, *Nature*, 347, 650  
 McLaughlin M. A. et al., 2006, *Nature*, 439, 817  
 Manchester R. N., Hobbs G. B., Teoh A., Hobbs M., 2005, *AJ*, 129, 1993  
 Morello V., 2016, MSc Thesis, Swinburne University of Technology  
 Morello V., Barr E. D., Bailes M., Flynn C. M., Keane E. F., van Straten W., 2014, *MNRAS*, 443, 1651  
 Osten R. A., Bastian T. S., 2008, *ApJ*, 674, 1078  
 Petroff E. et al., 2014, *ApJ*, 789, L26  
 Petroff E. et al., 2015, *MNRAS*, 451, 3933  
 Petroff E. et al., 2016, *PASA*, 33, 45  
 Price D. C., Staveley-Smith L., Bailes M., Carretti E., Jameson A., Jones M. E., van Straten W., Schediwy S. W., 2016, *J. Astron. Instrum.*, 5, 1641007  
 Radakrishnan V., Cooke D. J., 1969, *Astrophys. Lett.*, 3, 225  
 Ransom S. M., 2005, *Science*, 307, 892  
 Ransom S. M., Eikenberry S. S., Middleditch J., 2002, *AJ*, 124, 1788  
 Raza J., van der Veen A. J., 2002, *IEEE Signal Process. Lett.*, 9, 64  
 Rickett B. J., 1970, *MNRAS*, 150, 67  
 Robinson C., Lyne A. G., Manchester R. N., Bailes M., D'Amico N., Johnston S., 1995, *MNRAS*, 274, 547  
 Roy J., Gupta Y., Pen Ue-Li., Peterson J. B., Kudale S., Kodilkar J., 2010, *Exp. Astron.*, 28, 25

<sup>7</sup> <https://data.csiro.au>

- Sokolowski M., Wayth R. B., Morgan L., 2015, Proc. GEMCCON, 2015 IEEE Global  
 Spitler L. G. et al., 2016, Nature, 531, 202  
 Staelin D. H., 1969, IEEE Proc., 57, 724  
 Staveley-Smith L., 1996, PASA, 13, 243  
 Tauris T. M., Savonije G. J., 1999, A&A, 350, 928  
 Thornton D. et al., 2013, Science, 341, 53  
 Tingay S. J. et al., 2013, PASA, 30, 7  
 van Straten W., 2013, ApJS, 204, 13  
 van Straten W., Manchester R. N. Johnston S., Reynolds J. E., 2010, PASA, 27, 104  
 Williams P. K. G., Berger E., 2016, ApJ, 821, L22  
 Yao M. J., Manchester R. N., Wang N., 2017, ApJ, 835, 29

## SUPPORTING INFORMATION

Supplementary data are available at [MNRAS](https://academic.oup.com/mnras/article/473/1/116/4083641) online.

### List\_of\_SUPERB\_Pointings.csv

Please note: Oxford University Press is not responsible for the content or functionality of any supporting materials supplied by the authors. Any queries (other than missing material) should be directed to the corresponding author for the article.

This paper has been typeset from a  $\text{\LaTeX}$  file prepared by the author.